

**NASA  
Technical  
Memorandum**

NASA TM- 103518

**DENDRITIC MORPHOLOGY AND MICROSEGREGATION  
IN DIRECTIONALLY SOLIDIFIED SUPERALLOY,  
PWA-1480, SINGLE CRYSTAL: EFFECT OF GRAVITY—  
CENTER DIRECTOR'S DISCRETIONARY FUND REPORT**

By S.N. Tewari, M. Vijaya Kumar, J.E. Lee, and P.A. Curreri

Materials and Processes Laboratory  
Science and Engineering Directorate

November 1990

(NASA-TM-103518) DENTRITIC MORPHOLOGY AND  
MICROSEGREGATION IN DIRECTIONALLY SOLIDIFIED  
SUPERALLOY, PWA-1480, SINGLE CRYSTAL: EFFECT  
OF GRAVITY; CENTER DIRECTOR'S DISCRETIONARY  
FUND REPORT (NASA) 56 p

N91-15391

Unclass

CSCL 11F G3/26 0325579



National Aeronautics and  
Space Administration

**George C. Marshall Space Flight Center**



1. Report No. <b>NASA TM-103518</b>		2. Government Accession No.		3. Recipient's Catalog No.	
4. Title and Subtitle <b>Dendritic Morphology and Microsegregation in Directionally Solidified Superalloy, PWA-1480, Single Crystal: Effect of Gravity—Center Director's Discretionary Fund Report</b>				5. Report Date <b>November 1990</b>	
				6. Performing Organization Code	
7. Author(s) <b>S.N. Tewari,* M. Vijaya Kumar,* J.E. Lee, and P.A. Curreri</b>				8. Performing Organization Report No.	
				10. Work Unit No.	
9. Performing Organization Name and Address <b>George C. Marshall Space Flight Center Marshall Space Flight Center, Alabama 35812</b>				11. Contract or Grant No.	
				13. Type of Report and Period Covered <b>Technical Memorandum</b>	
12. Sponsoring Agency Name and Address <b>National Aeronautics and Space Administration Washington, DC 20546</b>				14. Sponsoring Agency Code <b>NASA</b>	
15. Supplementary Notes <b>Prepared by Materials and Processes Laboratory, Science and Engineering Directorate</b>  <b>*Cleveland State University, Cleveland, Ohio 44115.</b>					
16. Abstract <p>Primary dendrite spacings, secondary dendrite spacings, and microsegregation have been examined in PWA-1480 single crystal specimens which were directionally solidified during parabolic maneuvers on the KC-135 aircraft. Experimentally observed growth rate and thermal gradient dependence of primary dendrite spacings are in good agreement with predictions from dendrite growth models for binary alloys. Secondary dendrite coarsening kinetics show a reasonable fit with the predictions from an analytical model proposed by Kirkwood for a binary alloy. The partition coefficients of tantalum, titanium, and aluminum are observed to be less than unity; while that for tungsten and cobalt are greater than unity. This qualitatively similar to their nickel base binaries. Microsegregation profiles experimentally observed for PWA-1480 superalloy show a good fit with Bower, Brody, and Flemings model developed for binary alloys. Transitions in gravity levels do not appear to affect primary dendrite spacings. A trend of decreased secondary arm spacings with transition from high gravity to the low gravity period was observed at a growth speed of <math>0.023 \text{ cm s}^{-1}</math>. However, definite conclusions can only be drawn by experiments at lower growth speeds which make it possible to examine the side-branch coarsening kinetics over a longer duration. Such experiments, not possible due to the insufficient low-gravity time of the KC-135, may be carried out in the low-gravity environment of space.</p>					
17. Key Words (Suggested by Author(s)) <b>Microsegregation, Primary Dendrite Spacings, Secondary Dendrite Spacings, Superalloy, Binary Alloy, Partition Coefficients, Gravity, Directional Solidification, Solute, Eutectic</b>				18. Distribution Statement  <b>Unclassified – Unlimited</b>	
19. Security Classif. (of this report) <b>Unclassified</b>		20. Security Classif. (of this page) <b>Unclassified</b>		21. No. of pages <b>55</b>	
				22. Price <b>NTIS</b>	

## **ACKNOWLEDGEMENT**

This work was funded by the Marshall Space Flight Center, Center Director's Discretionary Fund, CDDF-87-14, under a cooperative agreement (NAG 8-091). Research facilities in the Microgravity Materials Science Laboratory, NASA-Lewis Research Center, Cleveland, were used during this study. Appreciation is expressed to G. Workman and G. Smith of the University of Alabama in Huntsville, and the personnel of the Johnson Space Center who operate the KC-135.

## TABLE OF CONTENTS

	Page
INTRODUCTION .....	1
EXPERIMENTAL.....	4
RESULTS.....	6
Microstructure and Alloy Characterization.....	6
Primary Dendrite Spacings .....	10
Effect of Gravity on Secondary Dendrite Arm Coarsening.....	12
Microsegregation .....	16
DISCUSSION .....	32
CONCLUSIONS.....	40
REFERENCES.....	45

## LIST OF ILLUSTRATIONS

Figure	Title	Page
1.	Calibration plot between raw “K-ratios” and the concentration values obtained from background corrected “K-ratios” .....	5
2.	PWA-1480 accelerometer, furnace position, and temperature data for a sample directionally solidified during the fifth high gravity parabola.....	7
3.	Thermal profiles near the liquidus temperature for PWA-1480 samples directionally solidified at $0.023 \text{ cm s}^{-1}$ .....	8
4.	Microstructure of directionally solidified PWA-1480. Growth speed = $0.001 \text{ cm s}^{-1}$ . Thermal gradient = $120 \text{ K cm}^{-1}$ .....	8
5.	Differential thermal analysis plot for PWA-1480. Cooling rate = $5 \text{ K/min}$ .....	10
6.	Effect of gravity on primary dendrite spacings measured along the length of PWA-1480 specimens directionally solidified at $0.023 \text{ cm s}^{-1}$ .....	11
7.	Effect of gravity transitions on primary dendrite spacings in a specimen directionally solidified at $0.013 \text{ cm s}^{-1}$ .....	13
8a.	Secondary dendrite arm spacing versus time plots for PWA-1480 directionally solidified at $0.013 \text{ cm s}^{-1}$ . Sample quenched during low gravity .....	14
8b.	Secondary dendrite arm spacing versus time plots for PWA-1480 directionally solidified at $0.013 \text{ cm s}^{-1}$ . Sample quenched during high gravity .....	14
9a.	Secondary dendrite arm spacing versus time plots for PWA-1480 directionally solidified at $0.023 \text{ cm s}^{-1}$ . Sample quenched during low gravity .....	15
9b.	Secondary dendrite arm spacing versus time plots for PWA-1480 directionally solidified at $0.023 \text{ cm s}^{-1}$ . Sample quenched during high gravity .....	15
10.	Comparison of the side-branch coarsening kinetics during directional solidification of PWA-1480 in low gravity and high gravity periods. Growth speed = $0.023 \text{ cm s}^{-1}$ .....	17

## LIST OF ILLUSTRATIONS (Continued)

Figure	Title	Page
11.	Composition at the outermost surface of the primary dendrite versus local interdendritic temperature .....	17
12.	Elemental x-ray distribution across primary dendrites in directionally solidified PWA-1480. Growth speed $\times 0.013 \text{ cm s}^{-1}$ .....	19
13a.	Microprobe beam paths across a typical dendrite .....	20
13b.	Distribution of Ta along the two paths traversed by the microprobe beam in Figure 13(a).....	20
14.	Tantalum isoconcentration contours across the primary dendrites at 1,550 K. Dendrite microstructure shown in the inset .....	21
15.	Transverse microstructures where detailed microsegregation analyses were completed. Growth speed = $0.001 \text{ cm s}^{-1}$ , $G = 120 \text{ K cm}^{-1}$ .....	23
16.	Equivalence between the fraction solid measured by area fractions in the isoconcentration contours and that given by "A" type paths .....	24
17.	Microsegregation of Ta, Ti, Al, Co, and W across the primary dendrites along "A" type of paths, 1,597 K.....	24
18a.	Superposition of Ta solutal profiles corresponding to 1,550 K and 1,605 K (for corresponding transverse sections in Fig. 15).....	25
18b.	Superposition of W solutal profiles corresponding to 1,550 K and 1,605 K (for corresponding transverse sections in Fig. 15).....	25
18c.	Scatter in composition versus fraction distance plot resulting from $\pm 5$ percent variation in the primary dendrite spacing .....	26
19a.	Superposition of Ta solutal profiles for the transverse microstructures in Figure 15 .....	28
19b.	Superposition of Ti solutal profiles for the transverse microstructures in Figure 15 .....	28
19c.	Superposition of Al solutal profiles for the transverse microstructures in Figure 15 .....	29

## LIST OF ILLUSTRATIONS (Concluded)

Figure	Title	Page
19d.	Superposition of Co solutal profiles for the transverse microstructures in Figure 15 .....	29
19e.	Superposition of W solutal profiles for the transverse microstructures in Figure 15 .....	30
20.	Thermal gradient and growth rate dependence of primary dendrite spacings in directionally solidified single crystal PWA-1480 .....	33
21.	Side-branch coarsening kinetics in PWA-1480.....	35
22.	Estimate of the contribution of solid-state diffusion to the microsegregation of Ti in PWA-1480 .....	36
23.	Variation of the $\bar{C}_s$ along the length of the primary dendrite protruding above the “eutectic” temperature.....	39
24a.	Comparison of the experimentally observed Ta microsegregation with the microsegregation predicted by the model of Bower, Brody, and Flemings.....	41
24b.	Comparison of the experimentally observed Ti microsegregation with the microsegregation predicted by the model of Bower, Brody, and Flemings.....	41
24c.	Comparison of the experimentally observed Al microsegregation with the microsegregation predicted by the model of Bower, Brody, and Flemings.....	42
24d.	Comparison of the experimentally observed Co microsegregation with the microsegregation predicted by the model of Bower, Brody, and Flemings.....	42
24e.	Comparison of the experimentally observed W microsegregation with the microsegregation predicted by the model of Bower, Brody, and Flemings.....	43



## LIST OF TABLES

Table	Title	Page
1.	Calibration statistics.....	6
2.	Effect of thermal gradient and growth rates on the primary arm spacing of directionally solidified superalloy PWA-1480 .....	8
3.	Solutal partition coefficients of PWA-1480.....	31
4.	Solutal buildup at the dendrite tip .....	37



## TECHNICAL MEMORANDUM

# DENDRITIC MORPHOLOGY AND MICROSEGREGATION IN DIRECTIONALLY SOLIDIFIED SUPERALLOY, PWA-1480, SINGLE CRYSTAL: EFFECT OF GRAVITY— CENTER DIRECTOR'S DISCRETIONARY FUND REPORT

## INTRODUCTION

A complex branched dendritic microstructure is usually produced during solidification of alloys. Breakdown of a planar liquid-solid interface first results in the formation of cells, the fingers of solid protruding into the solidifying melt. Primary dendrites are produced when an increasing degree of constitutional supercooling in the intercellular region results in the formation of side-branches (secondary dendrites). Solute redistribution during dendritic solidification of metallic alloys produces localized chemical inhomogeneity over distances of the order of primary arm spacings. This microsegregation is responsible for the coring observed in the cast microstructures. Microsegregation and formation and size distribution of primary and secondary dendrites have been extensively studied because of their significant influence on mechanical properties. Experiments which involve partial directional solidification under steady-state growth conditions, with a positive thermal gradient in the melt and rapid quenching to retain the dendritic morphology and the solutal distribution, are ideally suited for detailed morphological and microsegregation studies. These experiments allow efficient examination of effects, such as the solute buildup in liquid at the tips of primary dendrites, the solid-state diffusion in the primary dendrite, the interaction among various solutes, and side arm coarsening kinetics.

Several models have been proposed in the literature for predicting the dependence of the primary dendrite spacing ( $\lambda_1$ ) in binary alloys on solidification rate ( $R$ ), thermal gradient in the melt at the liquid-solid interface ( $G_1$ ), and the solute content of the alloy ( $C_0$ ) [1-3]. Hunt [1], utilizing the approach taken by Bower, Brody, and Flemings [4] for modeling microsegregation for a primary dendrite array, obtained the following relationship for  $\lambda_1$ .

$$\lambda_1^2 = 4 \sqrt{2} [(G_c^l/G_c) - 1] (D_l/R) r_l \quad , \quad (1)$$

where  $D_l$  is the solute diffusivity in the melt and  $r_l$  is the radius at the tip of the primary dendrite. The solutal gradient in the melt at the dendrite tip,  $G_c^l$ , during steady-state directional solidification is related to the solute content of the melt at the dendrite tip,  $C_l$ , by the following relationship,

$$G_c^l = R C_l (k-1)/D_l \quad , \quad (2)$$

where  $k$  is the solute partition coefficient. Because of the assumptions of local equilibrium and constant thermal gradient, the interdendritic composition gradient,  $G_c$ , is taken to be equal to

$G_1/m_1$ , where  $m_1$  is the liquidus slope. Hunt used  $C_1$  and  $r_1$  predictions from the dendrite growth model of Burden and Hunt [5] in the above relationship, and showed that for a range of binary alloys, the experimentally observed primary arm spacings are proportional to  $G_1^{-0.5}$  and  $R^{-0.25}$  as predicted from equation (1). However, detailed quantitative comparisons showed that this approach underpredicts the experimentally observed primary dendrite spacings [3,6–8]. Trivedi [3] incorporated the  $C_1$  and  $r_1$  predictions from his model for an isolated paraboloidal dendrite in equation (1) to predict the thermal gradient and growth rate dependence of primary dendrite spacings. This approach showed a good quantitative agreement with the experimental data for succinonitrile-acetone [3] and other binary alloys [6]. While extensive  $G_1$ ,  $R$ , and  $\lambda_1$  data are available in the literature from directional solidification experiments on binary alloys, where actual thermal gradients were measured by thermocouples placed in the melt, such data for commercial alloys are very limited [9,10]. The feasibility of using the above models for quantitatively predicting the experimentally observed primary dendrite spacings in commercial multicomponent alloys is relatively unexplored.

It has been observed that the initial side-branch spacing near the dendrite tip is about two to three times the dendrite tip radius [11–13]. The spacing between neighboring side-branches is observed to increase with increasing distance from the dendrite tip. Several factors have been proposed in the literature, which may be responsible for the secondary arm coarsening. The coarsening may be due to the process of a simultaneous dissolution of smaller arms with sharper tip radii and growth of larger arms with less curvature [14,15]. It may be due to the process of dendritic separation, i.e., the secondary arm dissolving and detaching from the primary dendrite (due to the sharp curvature which reduces the local liquidus temperature) [15]. The coalescence of the neighboring side-branches can also lead to coarsening [16,17]. Measurements of the side-branch spacing from the tip of the primary dendrites to their base in the quenched mushy region of the microstructure have been used to obtain more insight into the side-branch coarsening mechanism [12,18].

The primary dendrite spacing and secondary dendrite coarsening are controlled by the solutal profile in the melt at the dendrite tip ( $G_c^1$ ) and in the interdendritic region ( $G_c$ ). These solutal profiles also determine the elemental microsegregation produced during directional solidification. Brody and Flemings [19] and Bower, Brody, and Flemings [4] treated an array of primary dendrites of binary alloy growing at steady state during directional solidification, and proposed a theoretical model for characterizing the microsegregation patterns. They incorporated limited solid-state diffusion, called “back-diffusion,” and predicted the solute profile as a function of the fraction solid from the dendrite tip to the eutectic-like region at the base of the primary dendrites. This model provided a limited agreement with the experimental observations in aluminum-copper alloy [4]. Clyne and Kurz [20] extended the Brody and Flemings model to growth conditions with large back diffusion. Kobayashi [21] has recently presented an exact analytical model, which incorporates the effect of solid-state diffusion. Yeum, Laxmanan, and Poirier [22] have evolved an efficient numerical technique, utilizing the approach taken by Brody and Flemings. Solari and Biloni [23] incorporated in the Bower, Brody, and Flemings model the solute buildup at the dendrite tip caused by the divergent solutal field due to the curvature, as given by Burden and Hunt [5], to predict the microsegregation. Their predictions were in close agreement with the experimentally observed solute profile across primary dendrites in a melt spun Al-4.5% Cu alloy ribbon [24]. Sarreal and Abbaschian [25] have attempted to incorporate the back diffusion, solute buildup at the dendrite tip and the undercooling of the eutectic isotherm to predict the microsegregation.

Extensive microsegregation research has been reported in the literature on simple binary alloys [19,25,26–30]. Some work has been carried out on the ternary alloys [31,32]. However, very few experiments have been reported in the literature, where a similar systematic microsegregation study has been carried out on complex multicomponent commercial alloys [33–36].

Several recent experiments have explored the effect of gravity on primary and secondary dendrite arm spacings. Reduced gravity has generally resulted in increased secondary arm spacings [37–40]. Directionally solidified polycrystalline MAR-M246 [17] tended to exhibit an increased secondary arm spacing in portions of the sample solidified during the low gravity maneuver of the KC-135 parabolic flight, as compared to the portion which was solidified during the high gravity. The side-branch coarsening analysis of MAR-M246 is further complicated because of the formation of carbide precipitates between the liquidus and eutectic temperatures. A recent microgravity experiment on an aluminum-copper alloy differed from the norm, showing decreased secondary arm coarsening kinetics [41]. Extended duration low gravity experiments have established that reduced convection causes increased primary dendrite spacings [42,43]. However, the exact mechanism by which this is brought about is not understood. It has recently been shown that the increased primary dendrite spacings observed in the low gravity grown aluminum-copper alloy sample can be explained if one replaces the alloy growth speed  $R$ , in equation 1, with an order of magnitude estimate of interdendritic fluid velocity [43]. We believe that convection in the melt affects the ratio,  $G_c'/G_c$ , and thus alters the primary dendrite spacings. Any change in  $G_c'/G_c$ , which alters the primary dendrite spacings, would also effect the side-branch spacing, the tip radius of primary dendrites and the microsegregation. In a KC-135 experiment on superalloy, PWA-1480, a trend of increasing primary dendrite spacings was observed to correlate with the transition from high gravity portion of the KC-135 aircraft flight to the low gravity ones [44]. However, it was felt that the results from this study were not definitive. There was a large scatter in the dendrite spacing values because of the polycrystalline nature of the specimens examined in that study. The thermal profiles during directional solidification were also not measured because of the lack of suitable instrumentation.

The present study had two objectives. The first purpose was to generate ground based understanding of dendritic morphology and microsegregation in a multicomponent complex commercial superalloy PWA-1480. The second purpose was to examine the influence of reduced convection on these phenomena. Since KC-135 flights are presently the only platform available to obtain the low gravity growth, the effect of gravity on the solidification behavior of this alloy was explored by performing directional solidification experiments during low and high gravity maneuvers on the KC-135. The superalloy, PWA-1480 [nominal composition, Ni-12Ta-10.4Cr-5Co-5Al-4W-1.5Ti (weight percent)], which is used as a single crystal turbine blade material in advanced gas-turbine aeroengines, was selected for this study for the following reasons. Despite its multicomponent nature, this alloy has solidification behavior which is very similar to a binary alloy. Unlike carbon containing superalloys, such as IN-100, there is no carbide precipitate formation (at a temperature between the liquidus and the eutectic temperatures) to complicate the microsegregation analysis. In addition, as seen in this study, the final solidification of PWA-1480 at the base of the primary dendrites occurs at nearly a constant temperature, similar to the isothermal eutectic solidification in a binary system.

## EXPERIMENTAL

Details of the Bridgman type directional solidification apparatus are presented in Reference 43. The hot zone in the furnace assembly is about 10-cm long and 1 cm in internal diameter. The water-cooled copper chill zone at the bottom end of the furnace is approximately 5 cm in length. Single crystal PWA-1480 cylindrical rods ([100] within  $\pm 8$  degrees of the growth direction) were remelted in flowing argon atmosphere in alumina crucibles (0.635 cm I.D. and 46-cm long), containing two Pt-Pt 13% Rh thermocouples located along the specimen length with a separation of about 0.5 cm. The sample was positioned in the furnace to allow approximately 5-cm length of the original 7-cm long bars to be remelted. After a 20-min thermal soak the sample was directionally solidified approximately 3.5 cm at growth rates in the range of  $10^{-3}$  to  $2.3 \times 10^{-2}$  cm/s. When the top thermocouple was at a predetermined temperature, usually near the liquidus temperature of the alloy, 1,610 K, the furnace was quickly raised and a water spray quench block was activated to rapidly quench the sample. Typical cooling rates of approximately 50 K/s were recorded during quench by the thermocouple located near the tips of the primary dendrites. Experiments were conducted on the ground and on the KC-135 aircraft during its low gravity (25 s duration, acceleration = 0.01 – 0.02 g) and high gravity (60 to 90 s, acceleration = 1.7 g) periods of parabolic maneuvers. Flight maneuvers and quench were synchronized to obtain samples with the longest possible portion of their mushy zone solidifying during either the low gravity or the high gravity periods. Assuming that the growth speed is identical to the specimen withdrawal speed, the distances from the quenched primary dendrite tips along the specimen length were correlated with the various high and low gravity periods of the flight.

The specimens were metallographically polished and etched (etchant by volume: 33 acetic acid, 33 nitric acid, 33 water and 1 hydrofluoric acid) to correlate microstructural features, such as the tip and base of primary dendrites, with the temperatures measured by the two thermocouples. The dendrite tip radius was measured for one sample by serial sectioning of the primary dendrites on longitudinal sections (parallel to the alloy growth direction), and fitting a parabola to the mid-section of the dendrite near its tip. Primary dendrite spacings were measured on transverse sections (perpendicular to the growth direction) to examine their variation along the specimen length. Primary dendrite spacings reported in this paper are equal to  $\sqrt{A/N}$ , where A is the specimen cross section area (transverse section) and N is the number of primary dendrites on that cross section. Depending on the growth conditions, 200 to 600 primary dendrites were observed and counted on the corresponding specimen cross sections (18.58 to 20.14 mm<sup>2</sup>). Secondary arm spacings were measured by averaging the distance between five adjacent side-branches on the longitudinal section (parallel to the alloy growth direction) of a primary dendrite as a function of distance from the dendrite tip. Each of the side-branch spacing data reported here is the average of secondary arm spacings from four or five primary dendrites. The melting and solidification behavior of the alloy was examined by differential thermal analysis (argon atmosphere, heating and cooling rates of 5 K/min).

An Applied Research Laboratory Model SEMQ electron probe microanalyzer was used to examine the microsegregation across the primary dendrites, in the quenched interdendritic melt, and ahead of the dendrite tips. Because of the very large amount of microprobe data required for this study, initially the ZAF (atomic number, absorption, and fluorescence) corrected concentration values, obtained from the microprobe measurements, were used to prepare a calibration scheme.

This calibration scheme was subsequently used for analyzing the raw microprobe data. The ratio of x-ray count rates for a particular element on the PWA-1480 superalloy sample to that on a pure elemental standard, referred to as the raw "K-ratio," was plotted against the concentration values obtained from the background corrected "K-ratios," using a MAGIC IV ZAF correction scheme [46] for approximately 200 points covering the concentration range of interest. Figure 1 shows a typical graph for tantalum. Similar plots (not shown here) were obtained for the other elemental constituents. The calibration statistics obtained from a linear least squares analysis of the data is presented in Table 1. This table also lists the calibration statistics obtained for the other elements, aluminum, titanium, cobalt, and tungsten. It is evident from the correlation coefficient values in this table that all the elements show a good linear relationship between the "K-ratio" and the corrected concentrations with a relative standard deviation (RSD) of less than 3 percent. This calibration procedure obviates the need for collecting the background x-ray count rates and carrying out the ZAF correction for all the points analyzed, thus saving over 75 percent of the instrument time, without any loss in the accuracy of the analysis.

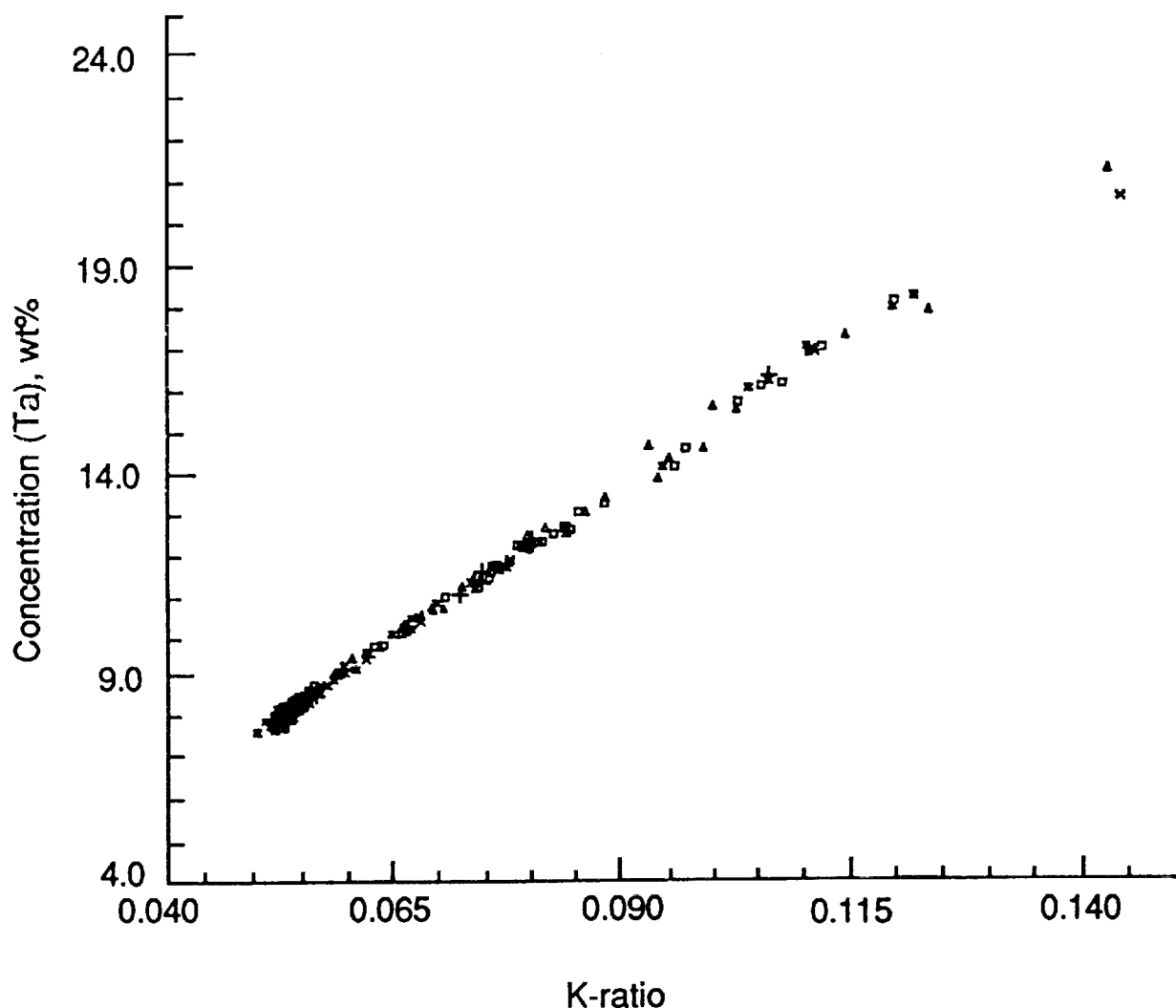


Figure 1. Calibration plot between raw "K-ratios: (ratio of x-ray count rate on PWA-1480 to that on a pure element) and the concentration values obtained from the background corrected "K-ratios" using MAGIC IV ZAF correction scheme for Ta.

TABLE 1. CALIBRATION STATISTICS

	Slope	Intercept	C.V.	R <sup>2</sup>
Al	173.194	-0.186	2.272	0.969
Ti	103.189	-0.161	2.797	0.997
Co	109.553	-1.134	1.455	0.966
W	162.918	-0.491	2.696	0.991
Ta	145.611	0.539	2.857	0.993

C.V.: Coefficient of variation; R<sup>2</sup>: Correlation Coefficient

## RESULTS

Figure 2 shows a typical time dependence of the accelerometer, furnace position, and sample temperature data for a sample which was directionally solidified at a speed of  $0.013 \text{ cm s}^{-1}$  and quenched during the fifth high gravity parabola. The thermal profiles from the two thermocouples are also shown in this figure. The thermal gradient ( $G_1$ ) in the melt at the tip of the primary dendrite array (assuming the tip temperature to be the liquidus temperature, 1,610 K) was obtained from similar temperature profiles. Table 2 lists the growth parameters of the specimens examined in this study. Figure 3 shows a typical comparison of the thermal profiles (temperature versus growth distance) in the vicinity of the mushy zone, as recorded by the lower thermocouples, during two different KC-135 experiments and the corresponding ground based experiment; all three with a growth speed of  $0.023 \text{ cm s}^{-1}$ . The specimen 1KC was quenched with its dendrite tips in the low gravity period. The other sample, 8KC, was quenched after one mushy zone length (cell length) had solidified during the high gravity period of the flight. The thermal profiles of the two specimens are nearly identical. The thermal gradients measured at the liquidus temperature from these plots are also similar:  $140 \text{ K cm}^{-1}$  (for 1KC) and  $150 \text{ K cm}^{-1}$  (for 8KC). Effect of gravity on side-branch coarsening kinetics will later be examined for these two samples. The three thermal profiles in Figure 3 appear similar. However, despite all the precautions it was not possible to reproduce an identical thermal profile for all experiments.

### Microstructure and Alloy Characterization

Figure 4 shows the microstructure of PWA-1480, directionally solidified at a crucible withdrawal speed of  $0.001 \text{ cm/s}$ . The longitudinal section parallel to the alloy growth direction (Fig. 4a) shows the well-aligned primary dendrites in the mushy zone. The experimentally observed length (cell length) of the primary dendrite arrays protruding into the melt vary from 0.4 to 0.6 cm. As will be seen later, good alignment of the primary dendrites with the growth direction is crucial to minimizing the scatter in the primary dendrite spacing and microsegregation data. The dendrite tips and the quenched liquid ahead of the tips can be clearly seen in this microstructure. The correlation of such a microstructure with the location of the top thermocouple at the time of



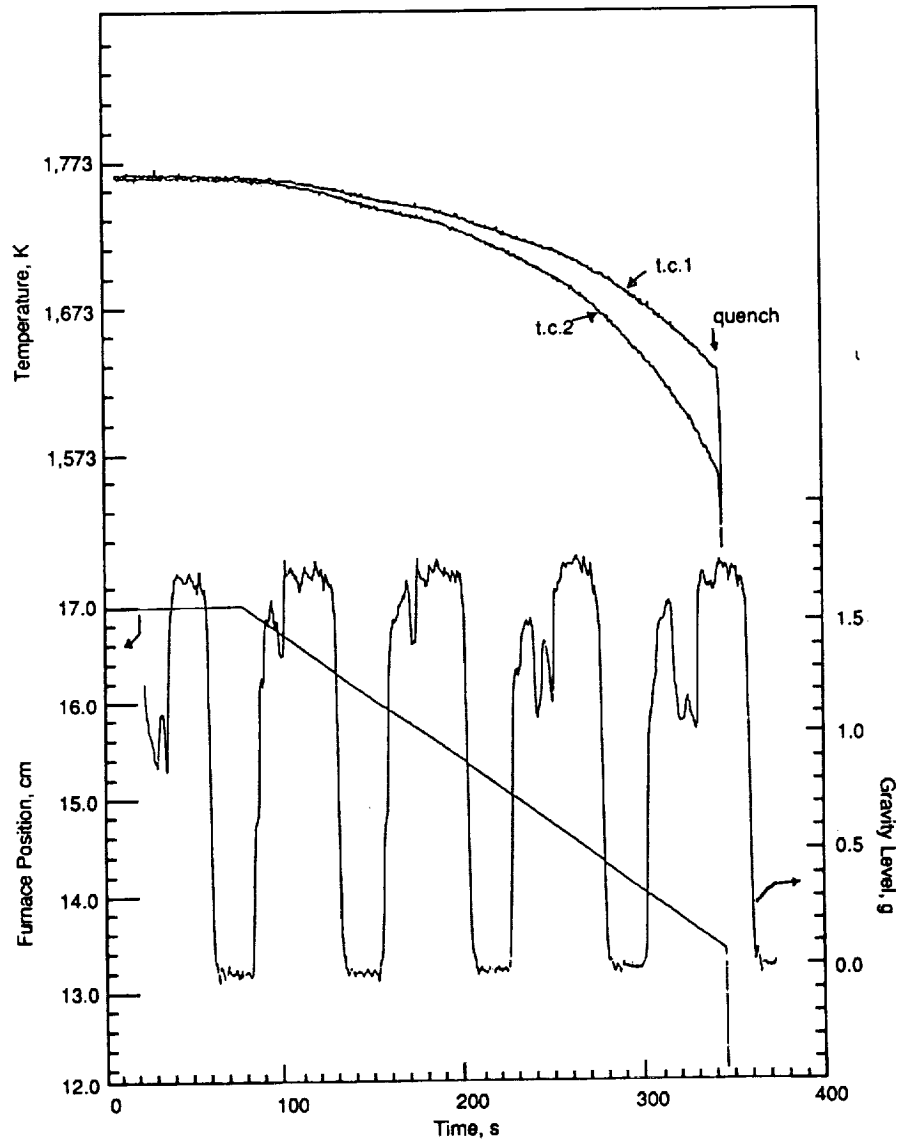


Figure 2. PWA-1480 accelerometer, furnace position, and temperature data for a sample directionally solidified at  $0.013 \text{ cm s}^{-1}$  during low and high gravity maneuvers and quenched during the fifth high gravity parabola.

quench and its adjacent thermal profile has shown the temperature at the tip of the primary dendrites to be about 1,610 K (between 1,605 and 1,610 K). The tip temperature thus measured is in agreement with the liquidus temperature of 1,610 K, measured for this alloy by the differential thermal analysis technique (Fig. 5). The location of the bottom thermocouple at the time of quench and its adjacent thermal profile was utilized to locate the interdendritic temperatures near the bottom of the primary dendrites. Figures 4b and 4c, corresponding respectively to 1,548 and 1,553 K, show the details of the interdendritic region in the microstructures on the transverse sections (perpendicular to the alloy growth direction). The interdendritic microstructure at 1,553 K is different from the one at 1,548 K. Large blocky eutectic gamma-prime nodules containing gamma phase (dark lines within the nodules) [47] were seen in the sample at locations corresponding to all the temperatures below 1,548 K. Whereas, fine gamma-gamma prime eutectic particles, as shown in Figure 4c, were observed in the quenched interdendritic regions corresponding to the temperatures higher than 1,553 K. An examination of the differential thermal analysis plot (Fig. 5) shows that the incipient melting occurs at about 1,550 K. A comparison of this incipient melting

TABLE 2. EFFECT OF THERMAL GRADIENT AND GROWTH RATES ON THE PRIMARY ARM SPACING OF DIRECTIONALLY SOLIDIFIED SUPERALLOY PWA-1480

Sample	R (cm/s)	G <sub>l</sub> (K/cm)	λ <sub>1</sub> (cm)
4GB	0.0033	120	0.0273
9GB	0.0100	85	0.0215
11GB	0.0133	90	0.0219
11KC	0.0233		0.0152
12GB	0.0017	100	0.0335
13GB	0.0010	120	0.0368
10GB	0.0067	120	0.0245
1KC	0.0233	140	0.0138
8KC	0.0233	150	0.0132
25GB	0.0233	180	0.0142
13KC	0.0133	150	0.0161
17KC	0.0133	170	0.0146
27GB	0.0133	110	0.0185

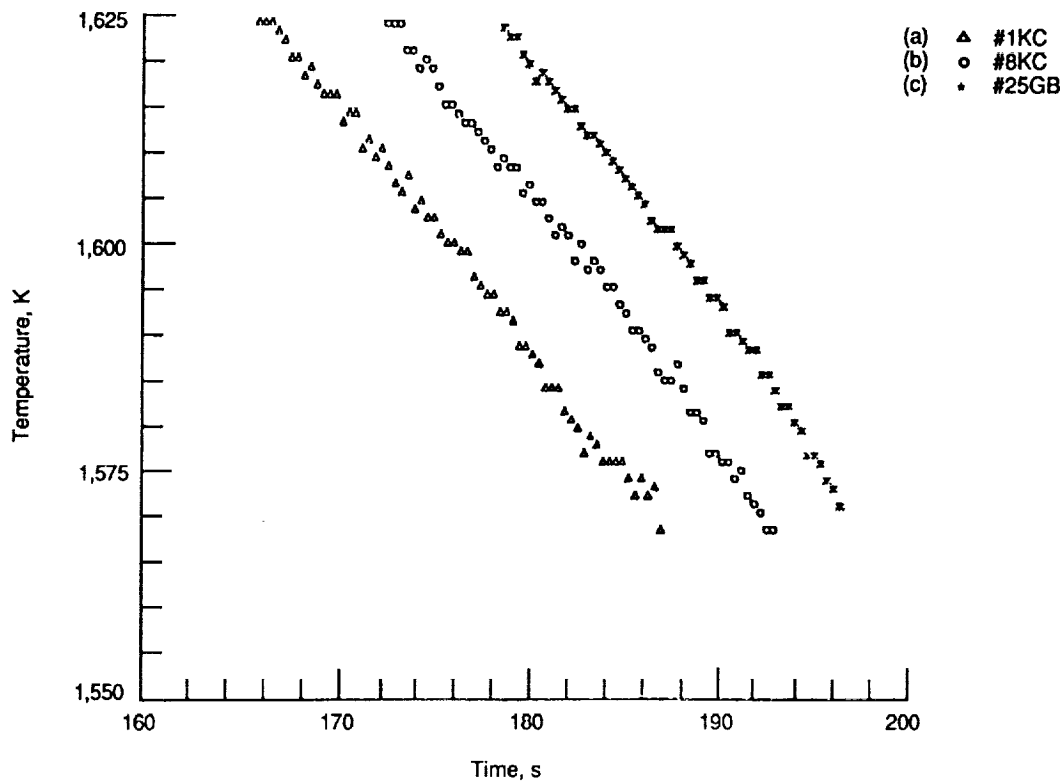


Figure 3. Thermal profiles near the liquidus temperature for PWA-1480 samples directionally solidified at  $0.023 \text{ cm s}^{-1}$  (a) specimen 1KC,  $G_l = 140 \text{ K cm}^{-1}$  quenched during low gravity period; (b) specimen 8KC,  $G_l = 150 \text{ K cm}^{-1}$ , quenched during high gravity period; and (c) specimen 25GB, solidified on the ground.

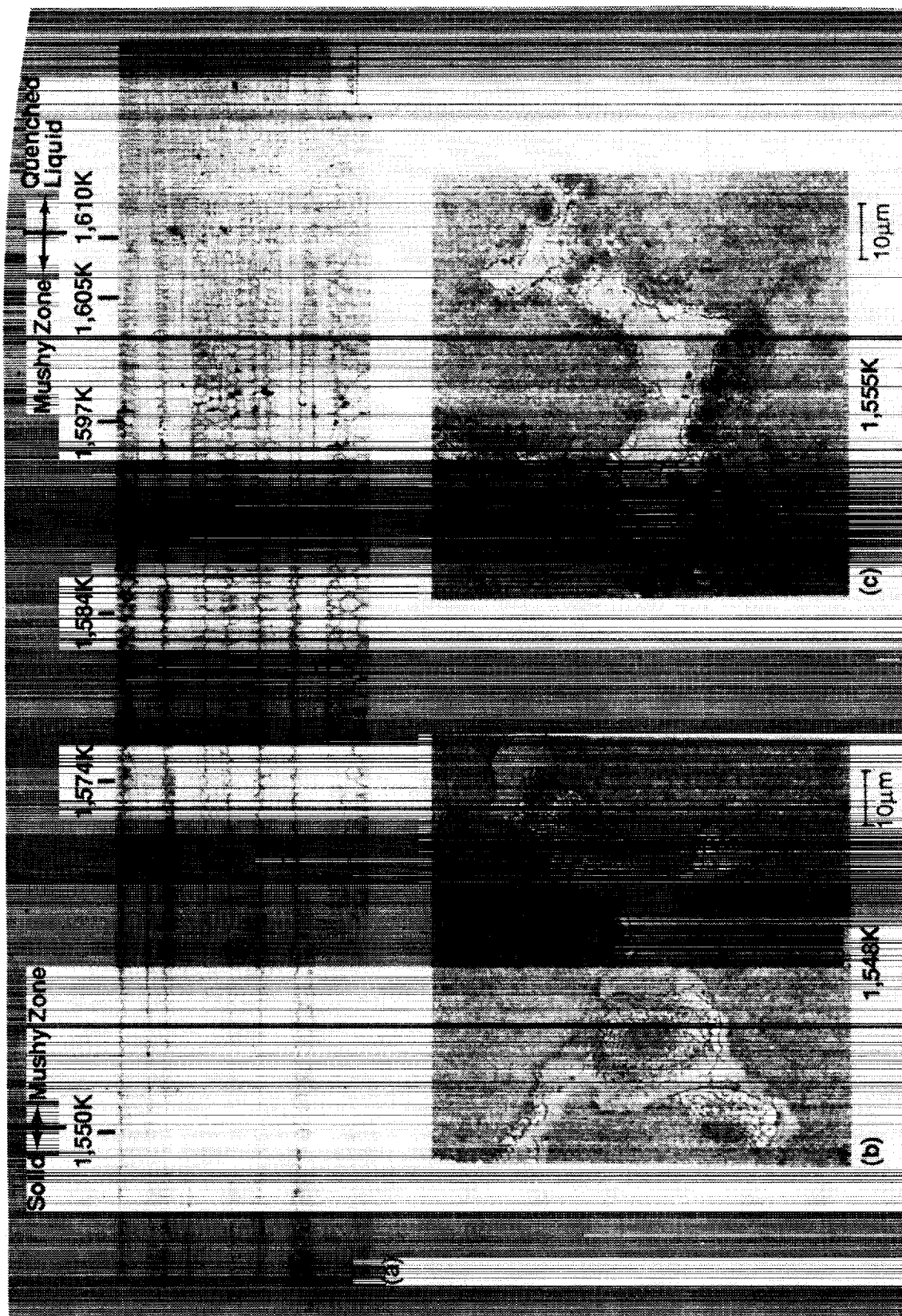


Figure 4. Microstructure of DS PWA-1480. Growth speed =  $0.001 \text{ cm s}^{-1}$ . Thermal gradient in the melt at the liquidus temperature =  $120 \text{ K cm}^{-1}$ . (a) Longitudinal section (parallel to growth direction), temperatures obtained from the thermal profiles are marked near the dendrite tips and the dendrite bases. (b) and (c) Transverse sections (perpendicular to the growth direction), near the base of the primary dendrites, at 1,548 K and 1,555 K.

ORIGINAL PAGE  
BLACK AND WHITE PHOTOGRAPH

ORIGINAL PAGE IS  
OF POOR QUALITY

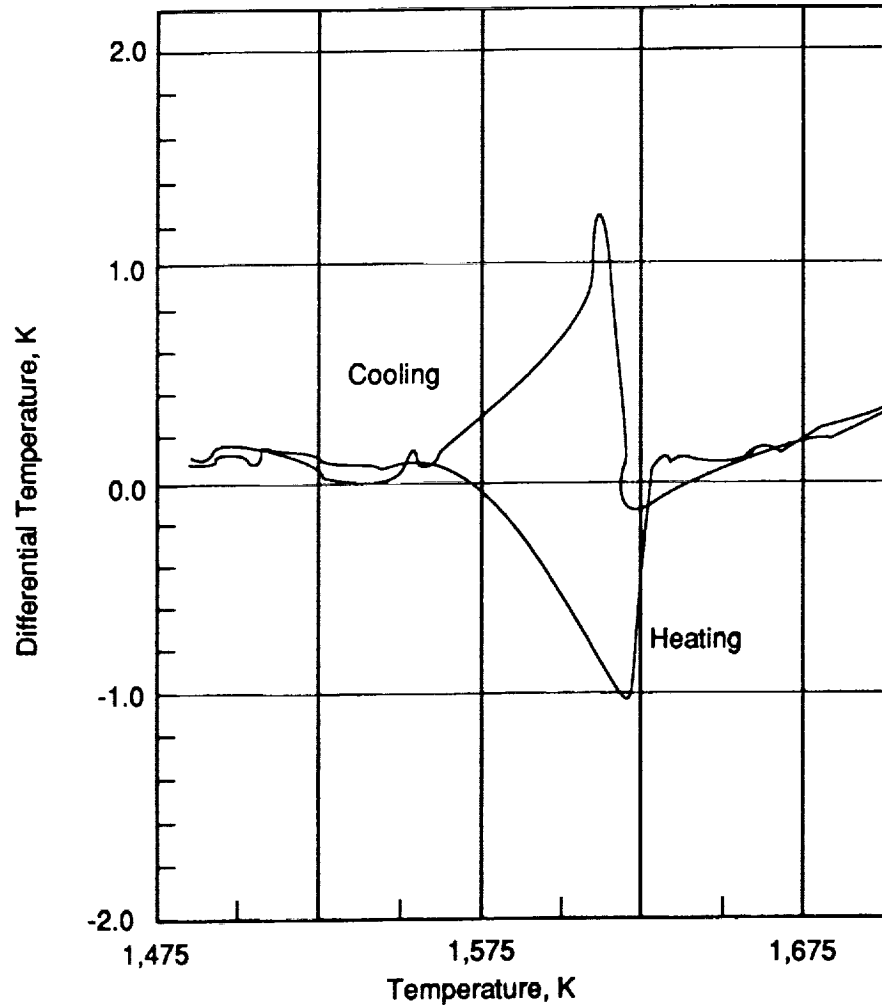


Figure 5. Differential thermal analysis plot for PWA-1480. Cooling rate = 5 K/min.

temperature with the observed microstructural difference between Figures 4b and 4c shows that the eutectic solidification in PWA-1480 occurs in a very narrow temperature range (approximately between 1,548 and 1,553 K, as per our measurements from the thermocouples imbedded in the directionally solidified specimen). It is interesting that PWA-1480, despite its complex multicomponent nature, appears to show a nearly isothermal (very narrow temperature range, 5 K) eutectic solidification. Such a solidification behavior is similar to that of the binary alloys, for which most of the theoretical models have been developed.

## Primary Dendrite Spacings

### Steady State Growth

Figure 6 plots the variation in primary dendrite spacing along the directionally solidified length of the three specimens which were grown at  $0.023 \text{ cm s}^{-1}$ . The thermal profiles for these specimens were shown in Figure 3. Distance "A" marked in this figure indicates the cell lengths

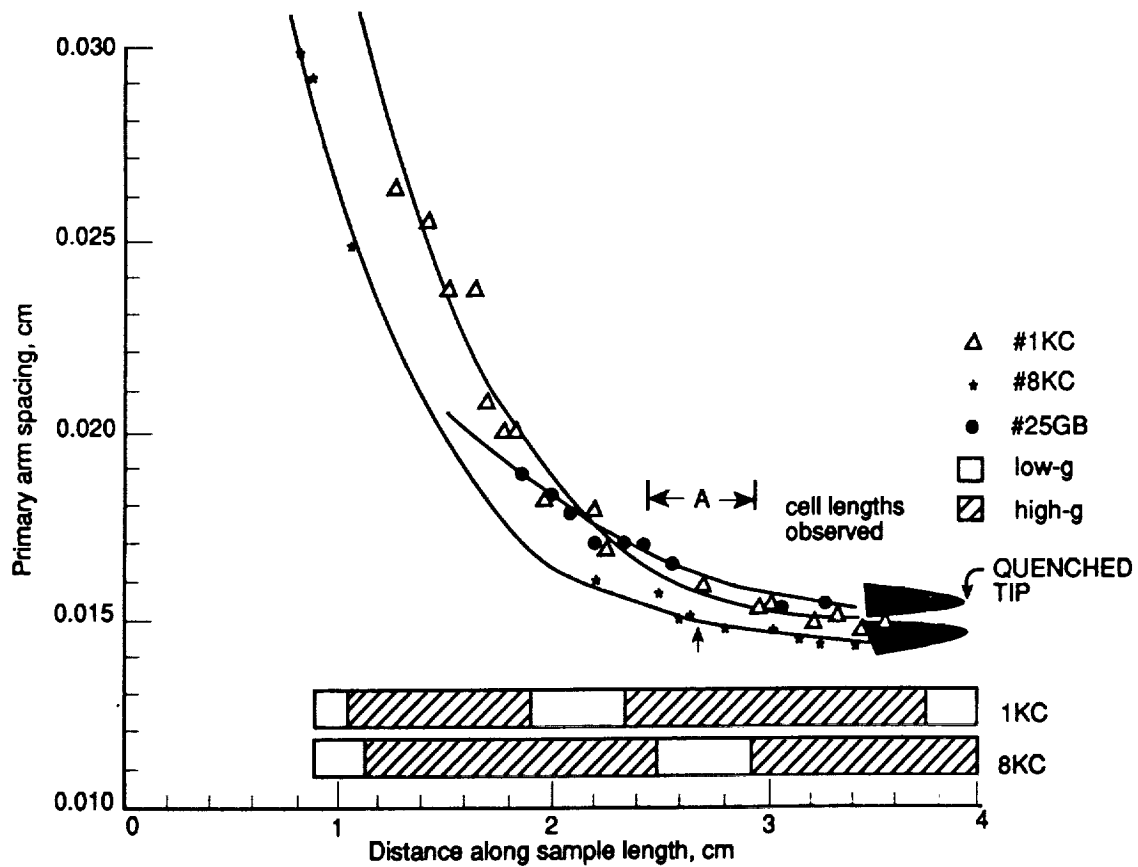


Figure 6. Effect of gravity on primary dendrite spacings measured along the length of PWA-1480 specimens directionally solidified at  $0.023 \text{ cm s}^{-1}$ .

observed in the three specimens (0.48, 0.45, and 0.45 cm for 1KC, 8KC, and 25GB, respectively). The quenched primary dendrite tips are schematically shown on the right hand side. Start of directional solidification is on the left side. This figure shows that initially the dendrite spacings decrease along the length of the solidifying specimens before becoming almost constant. This suggests that the growth conditions (specimen length: length of the melted and the solid portions of the bar, in relation to the furnace temperature profile), are not suitable to yield a steady-state growth along the full length of the sample. Assuming that the growth rate remains constant during solidification, an increasing thermal gradient with the distance solidified would result in such a decrease in the primary arm spacing. This initial increase in the thermal gradient can be understood as follows. When the solidification begins, there is approximately a 5-cm long melt column. The 1-cm long unmelted solid portion of the specimen fits loosely in the alumina crucible and does not provide an efficient heat extraction into the solid, resulting in a small thermal gradient in the solid at the solid-liquid interface. As more of the specimen length solidifies, the heat transfer into the solid becomes more efficient. It results in an increasing thermal gradient in the solid and the liquid. Nearly steady state growth conditions are subsequently achieved for a length which is approximately equal to two to three times the cell length, before the sample is quenched. This is indicated by reasonably constant dendrite spacing values near the quenched end of the specimen (Fig. 6). Primary dendrite spacings measured near the quenched end of the specimens (Table 2) have, therefore, been used in this study to obtain their quantitative dependence on thermal gradients and growth speeds.

## Effect of Gravity

Examination of 1KC and 8KC specimens in Figure 6 show that there is no significant change in primary dendrite spacings with transitions in gravity levels. The specimen, 1KC, was quenched when the primary dendrite tips were in the low gravity period of the flight. The specimen, 8KC, was quenched when its dendrite tips were in the high gravity period. The third is solidified on ground. The corresponding low gravity and high gravity periods for the two KC-135 samples are indicated at the bottom of this figure. These specimens do not show an increase in primary dendrite spacings in going from high gravity to low gravity periods of the flight, as was observed during an earlier study [44]. Since both the samples had nearly identical thermal profiles during solidification (as shown in Fig. 3), primary dendrite spacings in the two specimens can be compared at locations where one sample solidified during the low gravity period, whereas the other one solidified during high gravity (for example the portion marked by an arrow in Fig. 6). Within the experimental scatter, the low gravity grown portion in specimen 8KC has the same primary dendrite spacings, as the corresponding high gravity portion in 1KC. Specimens grown at  $0.013 \text{ cm s}^{-1}$  also did not show any significant variation in the primary dendrite spacings caused by gravity changes. This finding is contrary to the earlier observation where an 18 percent increase in the primary dendrite spacings corresponded with the transitions from high gravity to low gravity periods [44]. We do not understand the reasons for this anomaly. These experiments are different from the previous ones only in the following respects. The current specimens are single crystal (growth direction within about  $\pm 8^\circ$  of [100]) as compared to the earlier polycrystalline ones and are approximately twice as long.

The possibility that the thermocouple alumina sheaths (elliptical cross section with  $c/a = 0.2/0.12 \text{ cm}$ ), kept in the melt during these experiments, may somehow be responsible for modifying the response of the melt to the imposed gravity changes, was explored by directionally solidifying one sample at  $0.013 \text{ cm s}^{-1}$  without thermocouples. Results of the extensive primary dendrite spacing measurements along the length of this specimen are shown in Figure 7. The low gravity and high gravity periods of the growth are marked in this figure. Regions of the microstructure which correspond to the low- and high-gravity periods of the flight were identified in this specimen by correlating the furnace withdrawal with the initial melt-solid interface formed because of remelting. Unlike the previous observation [44], no abrupt primary dendrite spacing changes corresponding to the gravity level transitions are observed in the present study (Fig. 7).

## Effect of Gravity on Secondary Dendrite Arm Coarsening

Figures 8 and 9 show the secondary arm spacing versus time (distance from the dendrite tip divided by growth speed) plots for specimens which were grown during KC-135 flights at  $0.013$  and  $0.023 \text{ cm s}^{-1}$ , respectively. The high gravity ( $g_h$ ) and low gravity ( $g_l$ ) periods are also marked in these figures. The portions near the quenched end, showing the increasing secondary arm spacings from the tips of primary dendrite, along the cell length, can be used to obtain side-branch coarsening kinetics. The cell lengths observed in these specimens are schematically shown in these figures (lower right). Even for the specimen grown at our fastest growth rate,  $0.023 \text{ cm s}^{-1}$ , the entire low gravity period (approximately 25 s) is required to obtain the growth of one complete length of the primary dendrite array (0.48 cm). Because of the experimental difficulty in obtaining an exact synchronization among furnace withdrawal, flight parabolic maneuvers, and quenching,

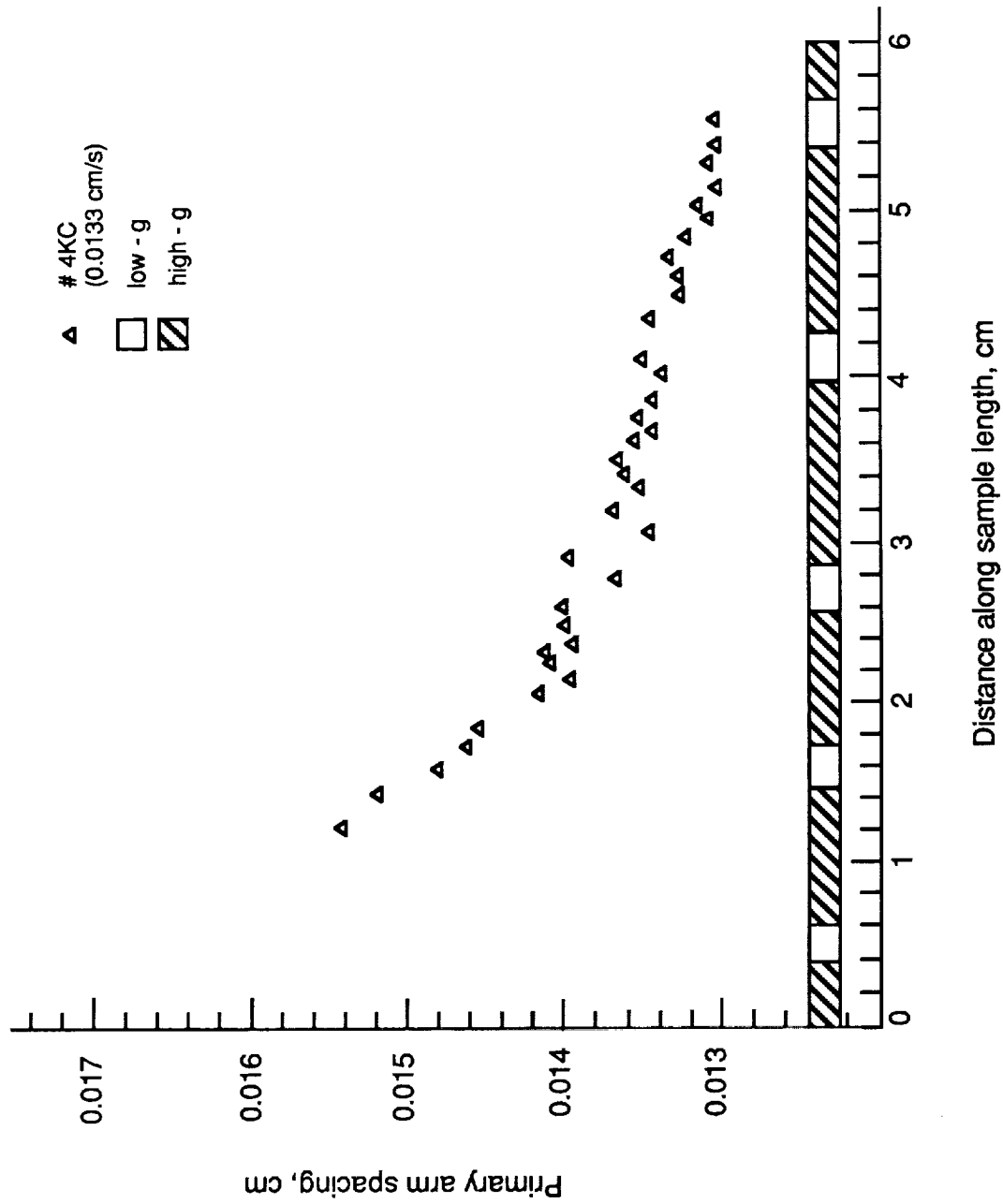


Figure 7. Effect of gravity transitions on primary dendrite spacings in a specimen directionally solidified at  $0.013 \text{ cm s}^{-1}$ . Specimen did not contain thermocouples in the melt.

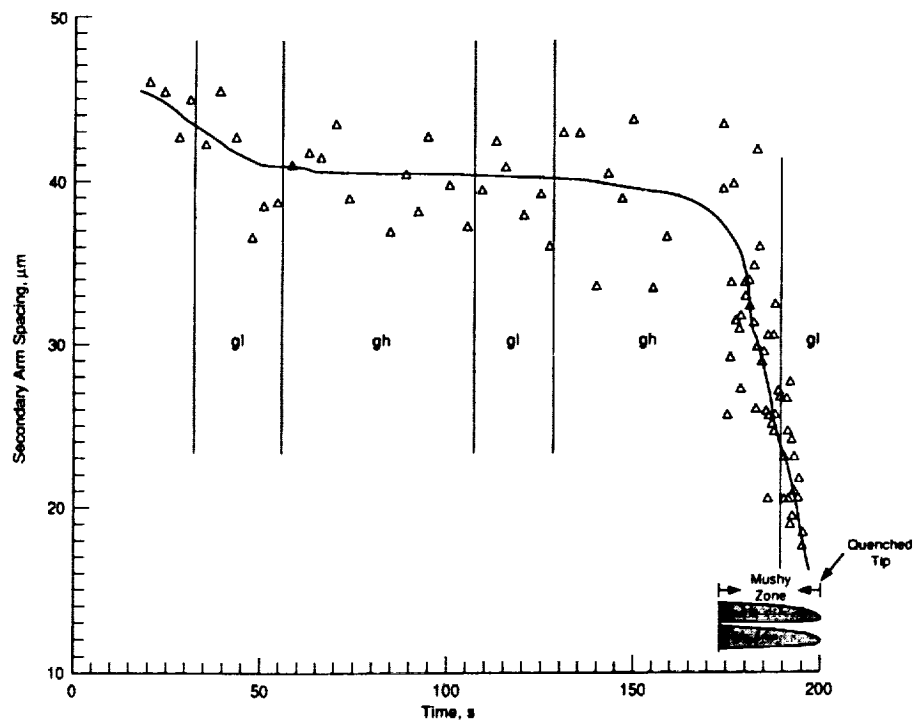


Figure 8a. Secondary dendrite arm spacing versus time plots for PWA-1480 directionally solidified at 0.013 cm s<sup>-1</sup>. Sample quenched during low gravity.

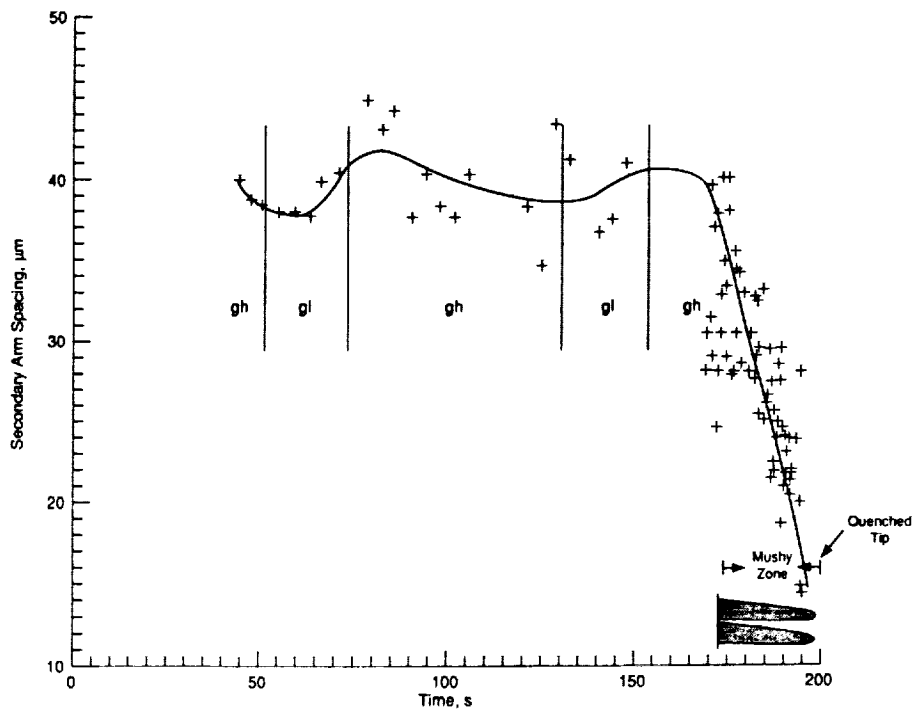


Figure 8b. Secondary dendrite arm spacing versus time plots for PWA-1480 directionally solidified at 0.013 cm s<sup>-1</sup>. Sample quenched during high gravity.



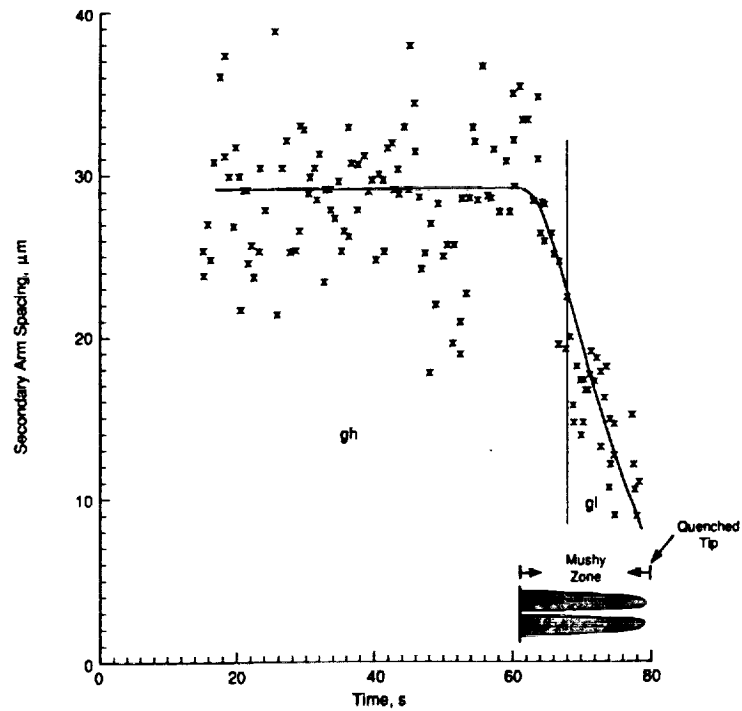


Figure 9a. Secondary dendrite arm spacing versus time plots for PWA-1480 directionally solidified at  $0.023 \text{ cm s}^{-1}$ . Sample quenched during low gravity.

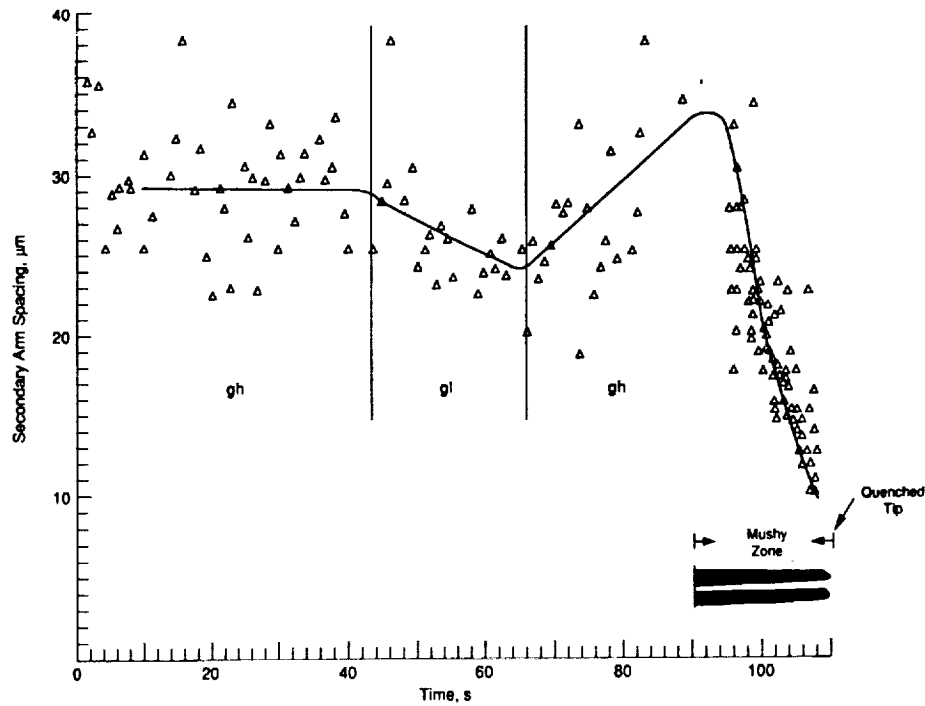


Figure 9b. Secondary dendrite arm spacing versus time plots for PWA-1480 directionally solidified at  $0.023 \text{ cm s}^{-1}$ . Sample quenched during high gravity.

and the need to ensure reproducible thermal profiles near the mushy zone, it was not possible to obtain specimens with one complete cell length formed during the low gravity period. Speeds higher than  $0.023 \text{ cm s}^{-1}$  were not used for the following reasons: (1) the scatter in the secondary arm spacing data became very large; (2) it was not possible to obtain a reproducible thermal profile; and (3) the previous experiments have shown decreasing influence of convection on dendrite spacing with increasing growth speed [37,44]. Side-branch coarsening along about 60 percent of the dendrite length occurred during the low gravity period of the flight for the sample grown at  $0.023 \text{ cm s}^{-1}$  (Fig. 9a). For the sample grown at  $0.013 \text{ cm s}^{-1}$ , only about 40 percent of the length near the dendrite tip had the side-branch coarsening occurring during low gravity. On the other hand the high gravity period (about 45 s) is sufficient to obtain the side-branch coarsening along the entire length of the primary dendrite (Figs. 8b and 9b). Figures 8 and 9 show that there is a large scatter in the data. The average behavior is shown by the solid lines in these figures. There does not appear to be any correlation in the observed secondary arm size and the gravity level for the specimens grown at  $0.013 \text{ cm s}^{-1}$  (Fig. 8). This may be due to the insufficient low gravity time; the high gravity portion of the parabola begins before the side-arms, initially formed near the tip of the primary dendrites in the beginning of the low gravity period, coarsen to their maximum possible size during that low gravity period. The specimen grown at  $0.023 \text{ cm s}^{-1}$  (Fig. 9b) appears to show a trend of decreasing secondary arm spacing with transition from high gravity to low gravity. This is contrary to the behavior earlier reported in the directionally solidified superalloy, Mar M-246, where an increase in the secondary arm spacing was noticed in going from high gravity periods of parabolic flight to low gravity periods [37]. The difference may be due to alloy dependent convective influences on initial dendrite arm spacing and on coarsening kinetics [17]. The scatter in the secondary arm spacing data is much larger in specimens grown at  $0.023 \text{ cm s}^{-1}$  as compared to that at  $0.013 \text{ cm s}^{-1}$ .

The initial data in Figures 9a and 9b have been replotted for the two specimens grown at  $0.023 \text{ cm s}^{-1}$  in Figure 10 as side-branch spacing versus coarsening time. Within the experimental scatter, the secondary arm coarsening kinetics appear to be the same for the high gravity and the low gravity periods. However, there is a large scatter in the data. As mentioned earlier the scatter in side-branch spacing data decreases with decreasing growth speeds. A more meaningful comparison of the effect of gravity on the side-branch coarsening kinetics in nickel base superalloys can be carried out only with similar partially directionally solidified and quenched specimens grown at much lower speeds, e.g.,  $0.001 \text{ cm s}^{-1}$  or less. The lower growth speeds would make it possible to examine the side-branch coarsening kinetics over a much longer time period. However, the low gravity period of the KC-135 parabolic flight is too short for this purpose. Such experiments should be carried out in the low gravity environment provided by the space shuttle, and the results compared with the samples grown under identical conditions on ground.

### Microsegregation

Figure 11 plots the average composition of the outermost region of the primary dendrites (as marked in the schematic figure) as a function of the temperature in the mushy zone. A linear temperature profile from the dendrite tip (1,610 K) to the base (1,550 K) was assumed in obtaining the temperatures corresponding to the distances from the tips. These compositions should correspond to the solute contents of the solid at the dendrite surfaces ( $C_s^*$ ) which are in equilibrium with the interdendritic liquid. There does not appear to be any significant variation in  $C_s^*$

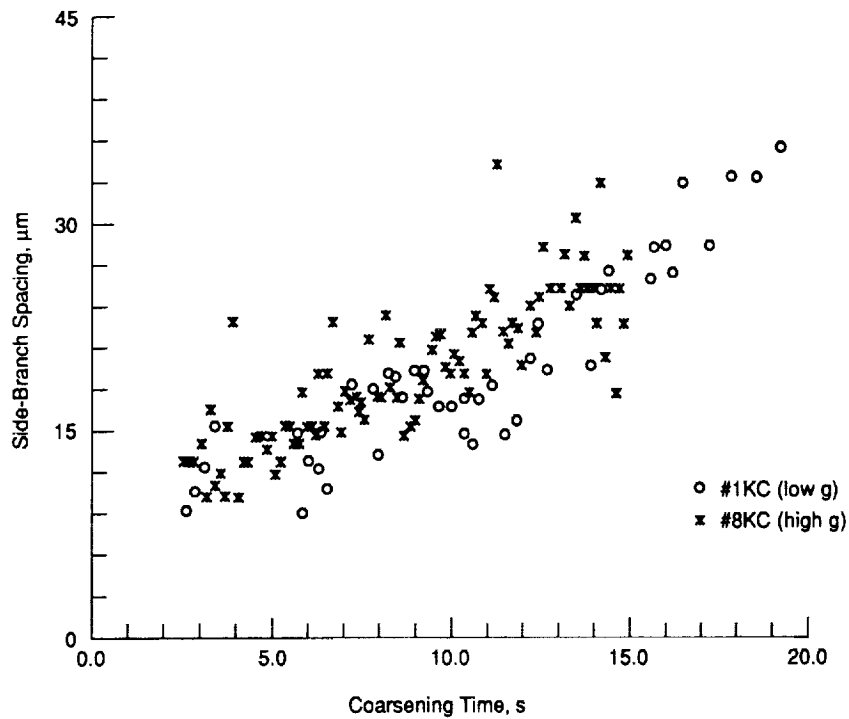


Figure 10. Comparison of the side-branch coarsening kinetics during directional solidification (growth speed =  $0.023 \text{ cm s}^{-1}$ ) of PWA-1480 in the low gravity and high gravity periods of the parabolic flight.

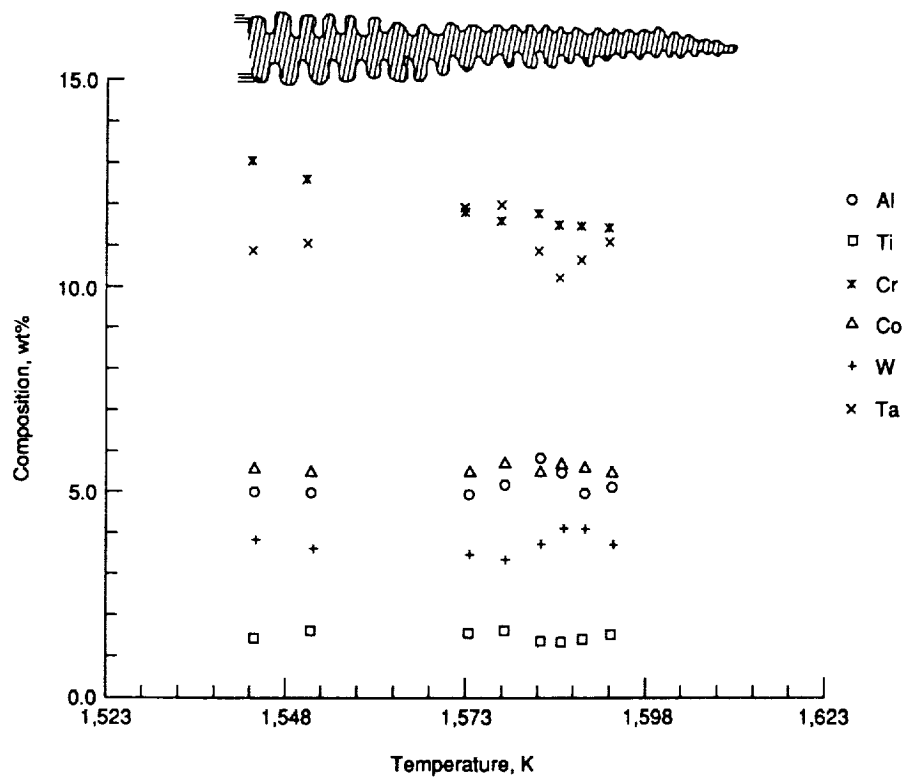


Figure 11. Composition at the outermost surface of the primary dendrite arm (the last solid to freeze) versus local interdendritic temperature.

from the base of the dendrite to its tip, for any of the six solute elements examined. This indicates the absence of any microsegregation. However, typical x-ray elemental distributions obtained on the transverse section of the directionally solidified alloy (Fig. 12) showed significant microsegregation. Figure 12 shows the elemental distributions of tantalum, titanium, and tungsten in the microstructure. The secondary electron image is at half the magnification of the x-ray images. It is evident that the dendrite core is richer in tungsten and poorer in tantalum and titanium than the interdendritic regions. The x-ray intensity distribution maps corresponding to cobalt, chromium, and aluminum did not show as much contrast, and are not shown here. It will be seen later that the apparent lack of microsegregation, based on the electron microprobe analysis along the length of the primary dendrite surface in the mushy zone, is due to the quenching artifacts.

**Accurate Representation of Fraction Solid ( $f_s$ ) in the Mushy Zone:** Experimental measurements of  $C_s^*$ , the solid composition at the dendrite surface in equilibrium with the interdendritic liquid, and the corresponding fraction solid,  $f_s$ , are necessary for quantitative study of microsegregation. Variation of the solute contents from the core of the primary dendrite ( $f_s = 0$ ) to the dendrite surface (the interface between the local interdendritic liquid solidified during the quench and the primary dendrite surface during the directional solidification), is dependent on the microstructural path traversed by the electron microprobe beam (Fig. 13a). Figure 13b shows the segregation profile for tantalum along the two typical paths shown in Figure 13a, which may be used to examine  $C_s^*$  versus  $f_s$ . The arrows on these paths in Figure 13a show the traverse direction of the electron beam. The core of the dendrite in Figure 13a is marked as "0." The ratio of the distance from the dendrite core to half of the dendrite outer dimensions along any of these paths could be used to represent  $f_s$ . The question arises as to which of these paths yields the most meaningful  $f_s$ . The smallest solute content of about 8 wt% tantalum observed in the dendrite core at "0" is also observed near the outer regions of the dendrite. It is evident that most of the solute buildup (for tantalum) occurs near the outer regions of the primary dendrite, which has a flower petal-like appearance in the transverse microstructure. Based on this information alone, it is not possible to select the most suitable path to measure  $f_s$ . The isoconcentration contours across the primary dendrites in the transverse microstructure of a directionally solidified specimen can be used to delineate the fraction solid and the corresponding  $C_s^*$ . However, this information alone cannot explain the extent of the back-diffusion occurring during directional solidification. Obtaining the isoconcentration contours on several transverse sections across the primary dendrite in the mushy zone would yield a measure of the extent of the solid-state diffusion, but would have required extensive use of instrument time for the microprobe analysis. Hence, the isoconcentration contours (Fig. 14) were obtained for only one dendrite, on one transverse section in the directionally solidified portion of the sample. This was very close to the base of the dendrite at 1,550 K. As shown below (Fig. 14), this analysis determined that the path marked "A" in Figure 13a is the most suitable traverse path for analyzing the microsegregation. Measurements were then made on three to four dendrites for a range of temperatures corresponding to transverse sections in the mushy zone to obtain the average solutal profiles.

Figure 14 shows the tantalum isoconcentration contours across the primary dendrite on a transverse section corresponding to 1,550 K. The numbers 1 to 8 correspond to the tantalum contents varying from 6 to 20 wt% as shown in the bottom of Figure 14. The microstructure of the dendrite is shown in the inset micrograph of Figure 14. The isoconcentration contours correspond to that quarter of the dendrite which is marked by points M, O, and N in the micrograph. The isoconcentration contours, shaped like one-quarter of a flower petal, are reasonably symmetrical.

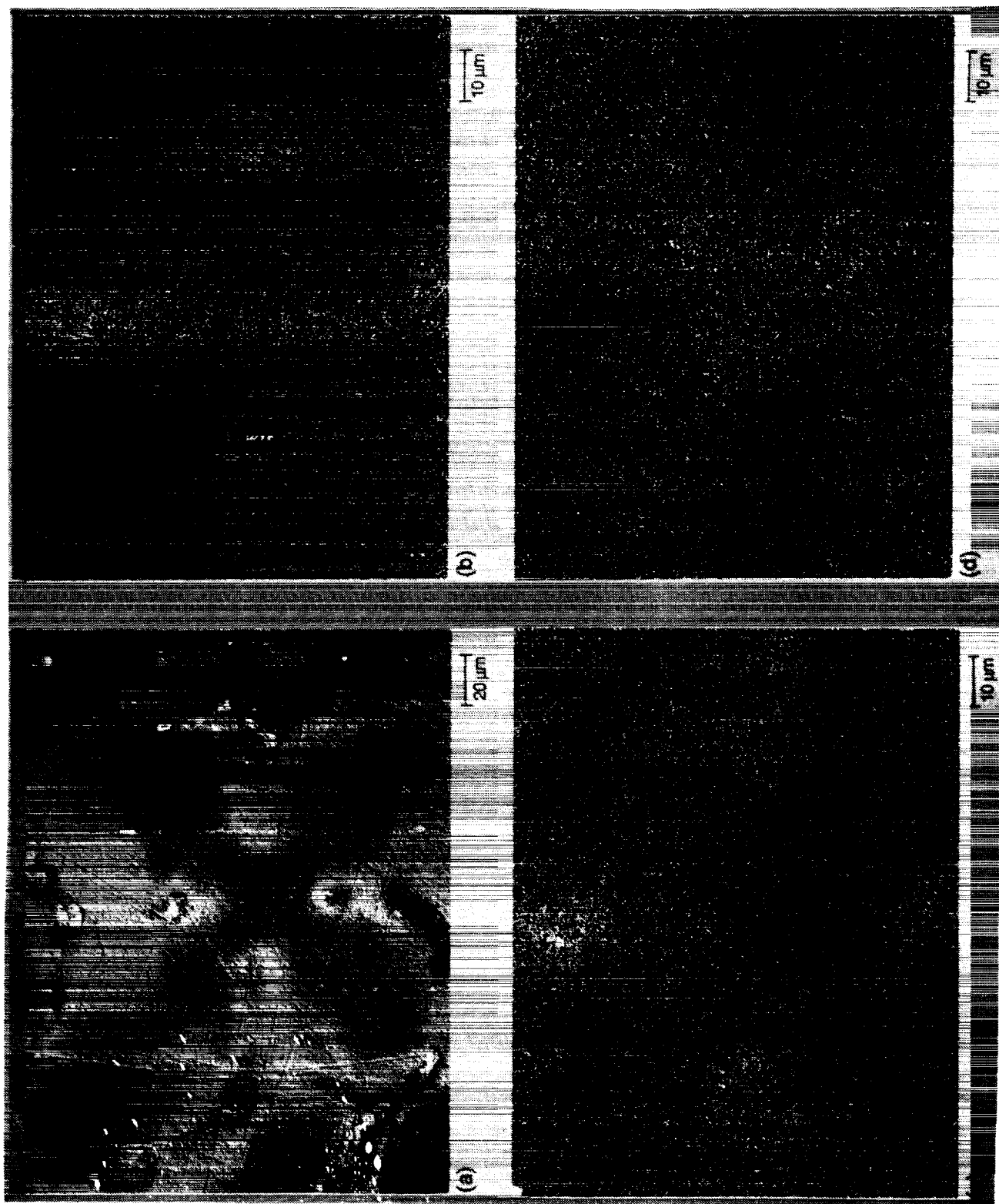


Figure 12. Elemental distribution (as indicated by the x-ray intensity distribution) across primary dendrites in directionally solidified PWA-1480. Growth speed =  $0.013 \text{ cm s}^{-1}$ . (a) Secondary electron image, (b) Ta, (c) Ti, and (d) W.

ORIGINAL PAGE  
BLACK AND WHITE PHOTOGRAPH



Figure 13a. Elemental distribution along the two paths traversed by the microprobe beam across a typical dendrite (transverse section). Microstructure and electron beam paths.

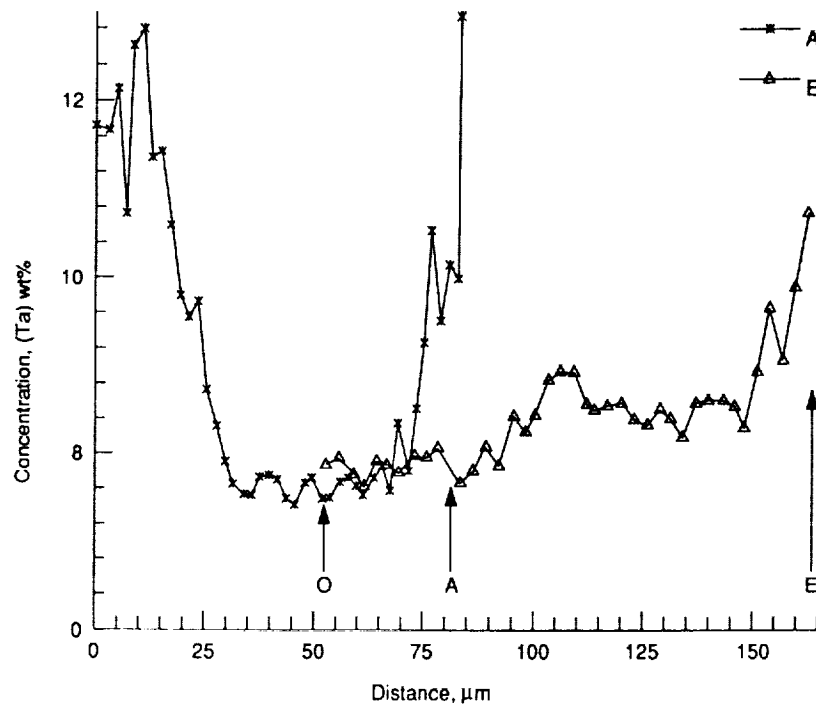


Figure 13b. Elemental distribution along the two paths traversed by the microprobe beam across a typical dendrite. Distribution of tantalum along the two paths shown in Figure 13a.

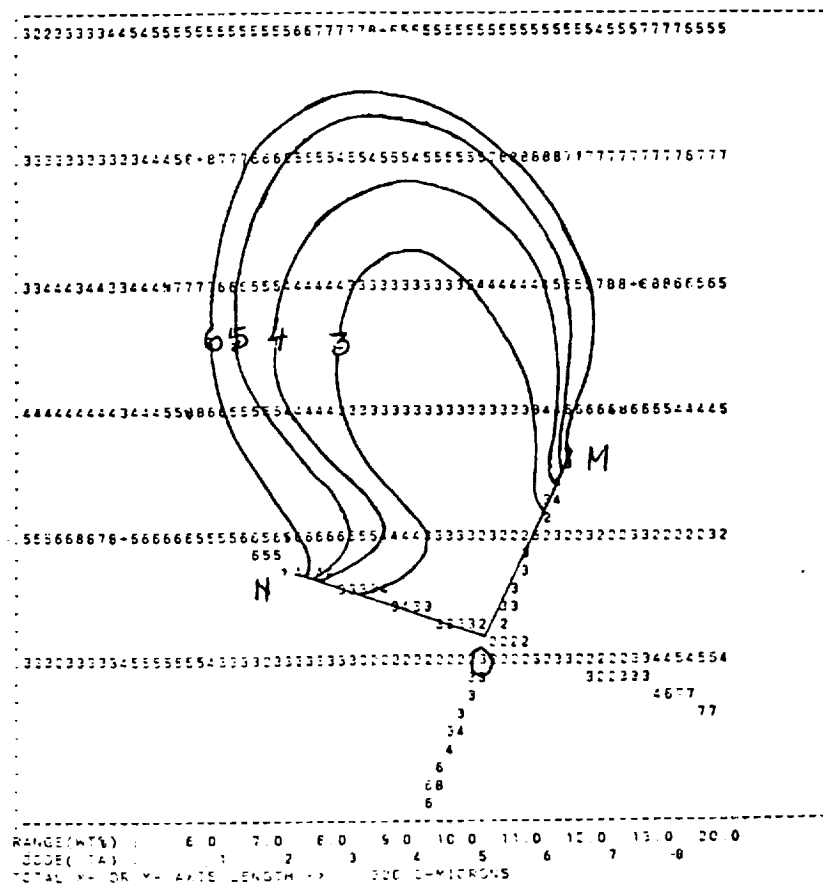
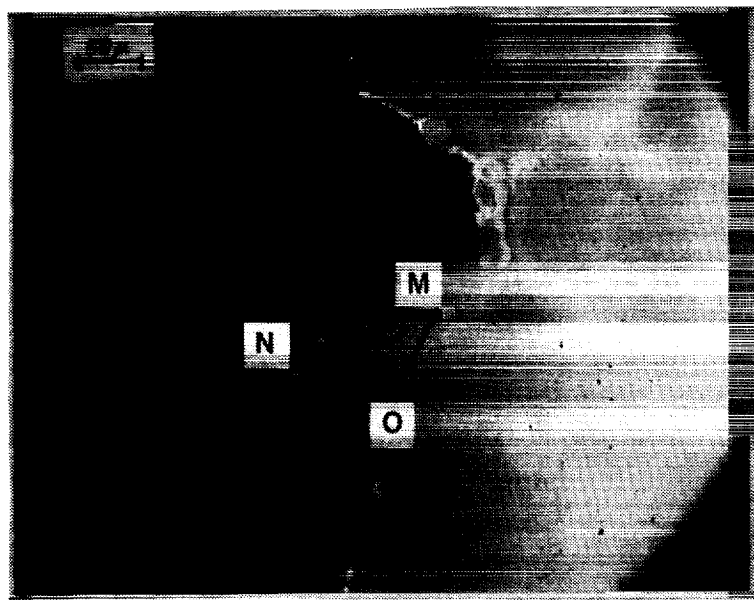


Figure 14. Tantalum isoconcentration contours across the primary dendrites at 1,550 K. Dendrite microstructure is shown in the inset. The quarter to which the isoconcentration contours correspond is shown by points M, N, and O in the inset micrograph.

This indicates that during solidification the transverse cross sections of the primary dendrites had similar shapes, while area fraction of the solid increased. This observation is also supported by the microstructural examination of the transverse sections of the primary dendrites along the length of the mushy zone (Fig. 15). The dendritic cross sections corresponding to the temperatures varying from 1,550 K to 1,610 K in the mushy zone have approximately the same flower petal-like shape with a four-fold symmetry.

Let us examine if the ratio  $R_1^2$  (the distance of the isoconcentrates along OM or ON from the dendrite core (point "O")/half the average distance between the two eutectic regions located opposite to each other, OM and ON)<sup>2</sup> can be used to represent the fraction solid,  $f_s$ . The points M and N are the mid points in the interdendritic eutectic region at the base of the primary dendrite, along the "A" type of the traverse path described earlier (Fig. 13). Figure 16 shows such a comparison, where the  $f_s$  values obtained from the area measurements (using isoconcentrates or transverse microstructures) are plotted with respect to those obtained from the "A" type of the paths (Fig. 13a). These  $f_s$  values compare well with the fraction solid data obtained from the ratio of the area contained within each of the isoconcentration contours (for example, shown as the hatched region) to the total area, total area being the sum of the interdendritic eutectic (about 9 percent by volume) and the outermost isoconcentrate in Figure 14. The filled circles in this figure denote the area fractions obtained by measuring the area of the transverse cross section of the primary dendrites in the microstructures shown in Figure 15. (For these very small fraction solid values it was not possible to draw the isoconcentrates in Figure 14 due to the very small difference between the dendrite core composition and the corresponding  $C_s^*$ ). Figure 16 shows that there is a one to one correspondence between the two previously discussed methods for obtaining  $f_s$ . The fraction solid ( $f_s$ ) values measured along paths similar to "A" shown in Figure 13 will be used in the rest of this paper.

## Microsegregation of Solutes in PWA-1480

Figure 15 shows the transverse sections and their corresponding temperatures for the primary dendrites on which extensive electron microprobe investigation has been completed. The corresponding longitudinal section is shown in Figure 4. The solutal profiles were obtained along "A" type paths on three to four dendrites, for the respective transverse sections, to obtain the average solute distributions. Figure 17 shows such solute profiles, starting from the interdendritic eutectic region at one end and terminating at the interdendritic eutectic region at the opposite end. For tantalum, aluminum, and titanium the solute contents increase from the core of the primary dendrite towards its periphery. This is the behavior expected for solutes with partition coefficients less than one. It is interesting to note that the nickel-based binaries for these three solutes have partition coefficients less than one [48]. On the other hand, cobalt and tungsten, with their partition coefficients based on nickel-based binaries greater than one, show an opposite trend. Their solute contents decrease going from the core of the dendrite cross section to the periphery. Chromium showed a reasonably uniform distribution across the primary dendrite and has not been studied in detail in this investigation.

Figure 18 shows the solute concentration versus the corresponding fractional distance from the dendrite center (core) relationships obtained from the elemental distributions, such as the ones shown in Figure 17. These fractional distances are based on half of the maximum distance between the two interdendritic eutectic regions located opposite to each other along "A" type paths in the



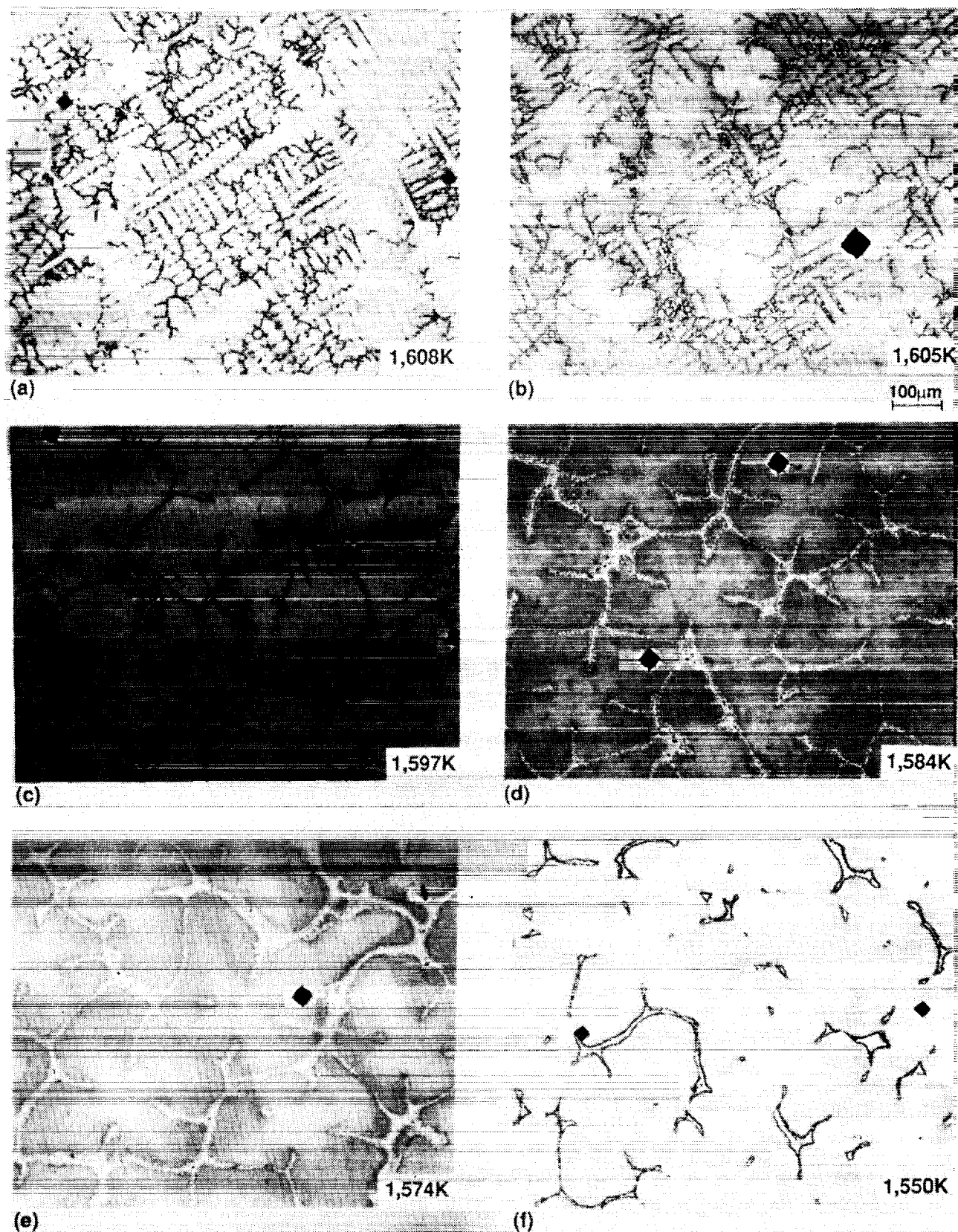


Figure 15. Transverse microstructures where detailed microsegregation analyses were completed. Growth speed =  $0.001 \text{ cm s}^{-1}$ ,  $G = 120 \text{ K cm}^{-1}$ . (a) 1,608 K, (b) 1,605 K, (c) 1,597 K, (d) 1,584 K, (e) 1,574 K, and (f) 1,550 K.

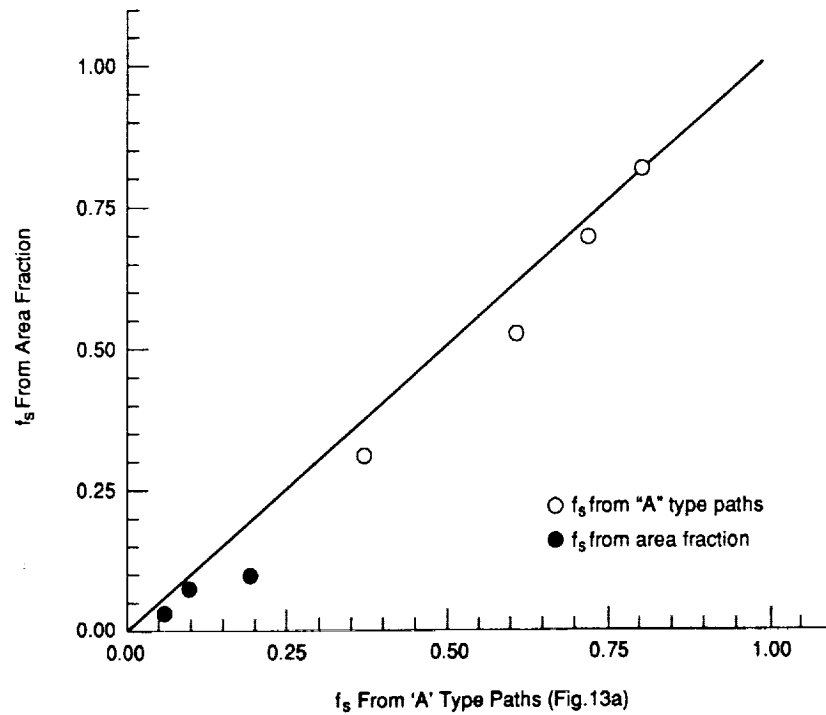


Figure 16. Equivalence between the fraction solidified,  $f_s$ , measured by area fractions in the isoconcentration contours and that given by "A" type paths (distance from the core of the primary dendrite/half the distance between opposite eutectic regions)<sup>2</sup>.

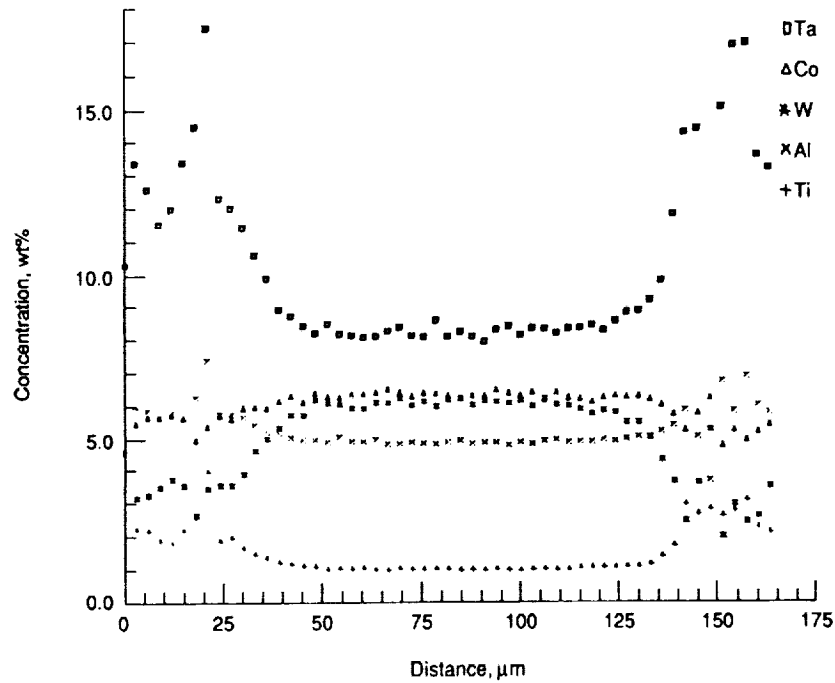


Figure 17. Microsegregation of Ta, Ti, Al, Co, and W across the primary dendrites along "A" type of paths, 1,597 K.

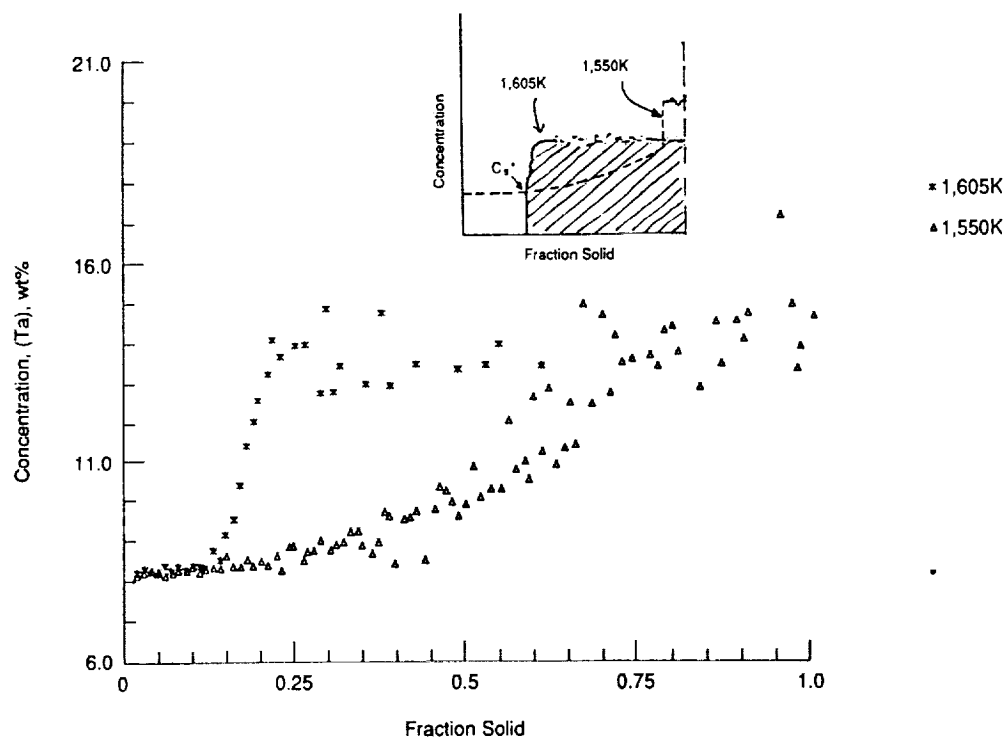


Figure 18a. Superposition of Ta solutal profiles corresponding to 1,550 K and 1,605 K (for corresponding transverse sections in Fig. 15). Inset figure shows how the solute partition coefficients,  $K = C_s^*/C_l$ , were obtained: where  $C_l$  is obtained by the average composition of the interdendritic melt (hatched area).

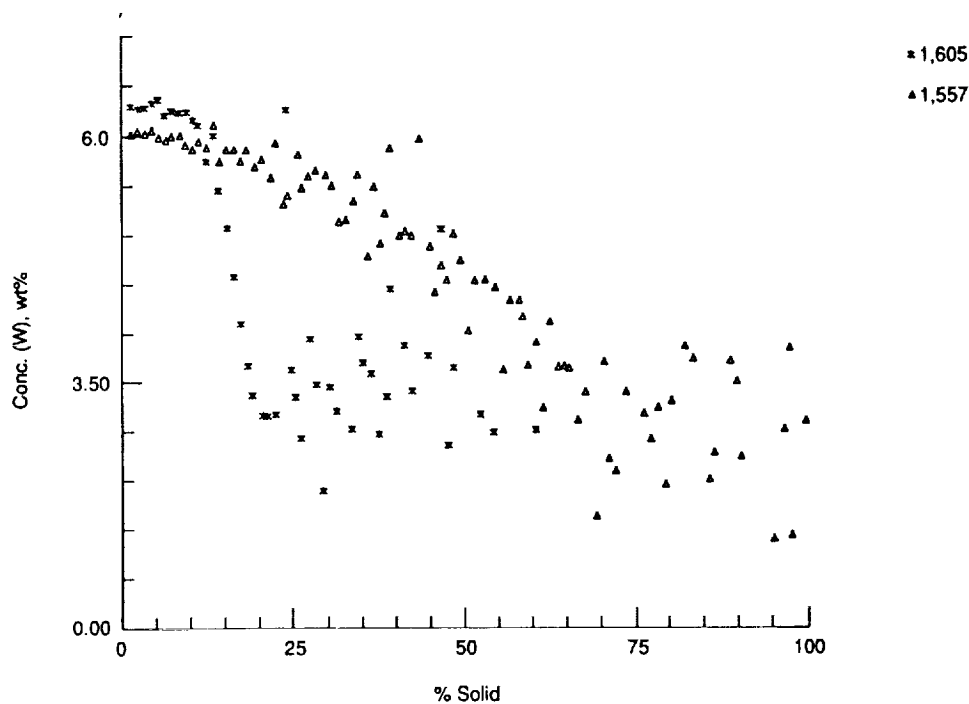


Figure 18b. Superposition of W solutal profiles corresponding to 1,550 K and 1,605 K (for corresponding transverse sections in Fig. 15).

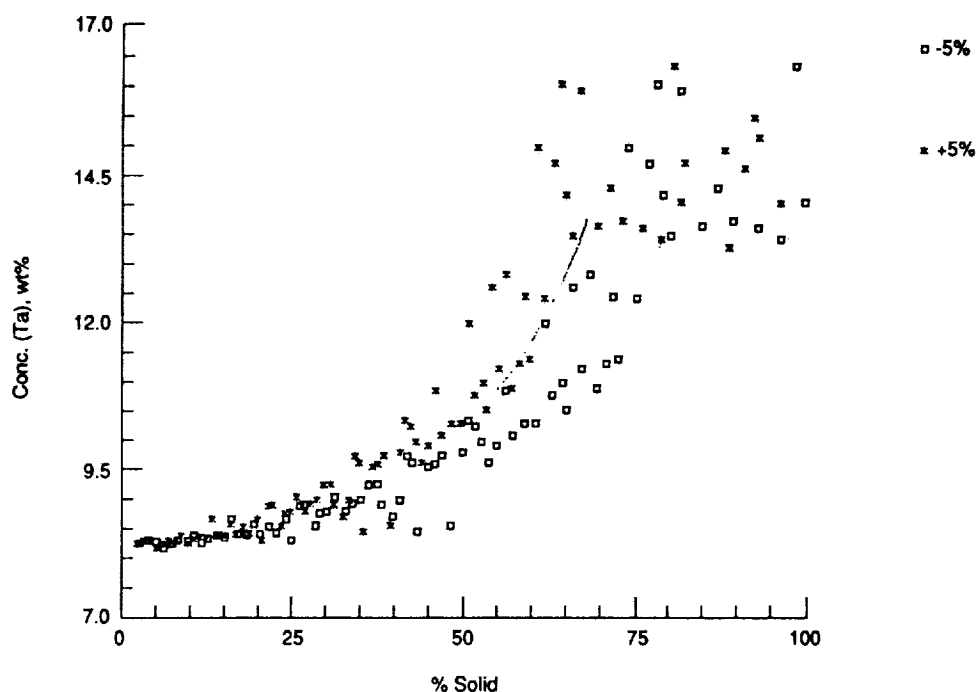


Figure 18c. Scatter in the composition versus fraction distance (solid) plot that would result from a  $\pm 5$  percent variation in the primary dendrite arm spacing.

transverse micrograph at the base of the primary dendrite. The elemental distributions were obtained on the two “A” type paths in each dendrite cross section. Typically three to four dendrites were examined for each of the transverse micrographs shown in Figure 15. Figure 18 shows the superposition of elemental profiles corresponding to 1,550 K at the base of the primary dendrites and 1,605 K near their tip. In this figure, we have selected the profiles for tantalum and tungsten to illustrate the typical behaviors of solutes with partition coefficients less than and greater than unity.

The solute profile for the cross section near the dendrite tip (1,610 K) is identical to the one obtained at the base of dendrite until about 30-percent fractional distance (Fig. 18). There is a steep change beyond this fraction solid. The solute content rapidly increases for tantalum and decreases for tungsten before reaching a region with a large amount of scatter in the data. This sharp change occurs within the primary dendrite arm near its outer surface. The scatter in the data is quite small initially at a small fractional distance. It increases with increasing fraction solid within the primary dendrite. However, it is very large in the region of the microstructure which corresponds to the quenched interdendritic melt.

The scatter in a plot, such as Figure 18, depends on the following factors: (1) the microprobe measurement process (instrument scatter), (2) the scatter due to local microstructural inhomogeneities larger than the probe x-ray resolution (approximately 3  $\mu\text{m}$ ), (3) an imperfect alignment of the primary dendrites with respect to the growth direction, and (4) the statistical variation in the primary dendrite arm size. The variation in the concentration values during the microprobe measurement occurs as a result of the fluctuations in the instrument settings and the

statistical nature of the x-ray counting process. As described earlier (Experimental section) the relative standard deviation due to this is about 3 percent (Table 1). This scatter of about +3 percent of the solute content is reasonable for this technique of electron microprobe analysis. The scatter due to the local microstructural variations is minimal within the primary dendrite, as is evidenced by about 3-percent scatter in the composition data near the core of the dendrites, closer to zero fraction distance (Fig. 18a). However, it is quite large (10 to 20 percent) in the quenched interdendritic liquid region of the microstructure. Here, the microstructure consists of discrete particles of gamma and gamma prime phases with very different compositions. The relatively large scatter in the composition profile (10 to 20 percent) is generated as the electron microprobe beam traverses these gamma and gamma prime phases. The scatter in the data also depends upon the degree of alignment of the primary dendrites with respect to the growth direction. A perfect alignment would result in a four-fold symmetry in the transverse microstructure of the dendrites. This would result in a symmetrical solute distribution along the opposite sides of the dendrite core along "A" type paths (as shown in Fig. 17). Otherwise the solute content at a given distance from the dendrite core on the one side would be different from the one at the same distance on the opposite side, causing the scatter in the solute concentration versus fraction solid (fraction distance) plots. Contribution from this scatter would be zero at the dendrite core, and would increase with increasing distance from the core. The scatter would be further enhanced when the data obtained from several primary dendrites with different alignments are superimposed. The fourth kind of scatter, due to the differences in the primary arm spacings, results from the errors in the fraction solid value calculated based on the average spacing near the eutectic isotherm, as has been done in this study. This effect is illustrated by Figure 18c, where the tantalum composition versus distance from the dendrite core data (shown in Fig. 17) have been replotted as composition versus percent solid (or  $(\text{fraction distance})^2 \times 100$ ). The two sets of data in Figure 18c, the average behavior indicated by the two curves, were generated by assuming the distance between the two opposing interdendritic regions at the base of the primary dendrite (such as shown in Fig. 13a), to be 5 percent greater and 5 percent less than the actual distance. As expected, the divergence between the two curves increases with the increasing fractional distance. This effect leads to a scatter in the concentration values when data for three to four analyzed dendrites are combined together, as is done in Figures 18, 19, and 24. The variation in the primary dendrite spacing in the directionally solidified superalloy PWA-1480 specimens is about 10 percent.

For the sake of clarity, the solutal profile data from the quenched interdendritic melt regions have been eliminated in Figure 19, where the superpositions of the solutal profiles from all of the transverse microstructures examined in the mushy zone (Fig. 15) are plotted for tantalum, titanium, aluminum, cobalt, and tungsten. All these transverse sections showed the steep change in the solute contents near the outer surface of the quenched primary dendrite. For each element the solute contents at the end of this steep change are nearly the same on all the cross sections examined in the mushy zone. This observation can explain the apparent absence of microsegregation seen earlier (Fig. 11), when the dendrite outer surfaces in the mushy zone were analyzed on the longitudinal sections. Apparently during quenching the initial solidification of the interdendritic liquid occurs by further growth of the preexisting gamma phase primary dendrite instead of independent nucleation of fine gamma dendrites, as is the case in the melt ahead of the mushy zone. During this process the interdendritic melt composition reaches the eutectic composition before the coupled eutectic solidification of the gamma and gamma prime phases. This results in an incorrect microsegregation observation on the longitudinal section: an apparently uniform composition in the interdendritic region from the base of the primary dendrite to near its tip. Therefore, in general, the longitudinal

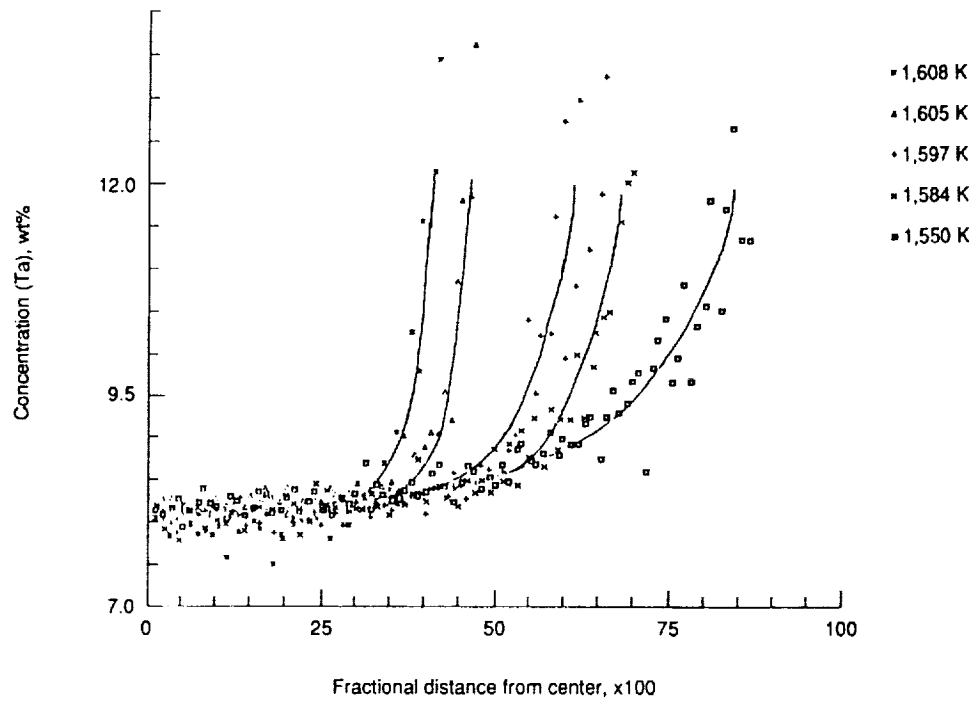


Figure 19a. Superposition of Ta solutal profiles for the transverse microstructures shown in Figure 15.

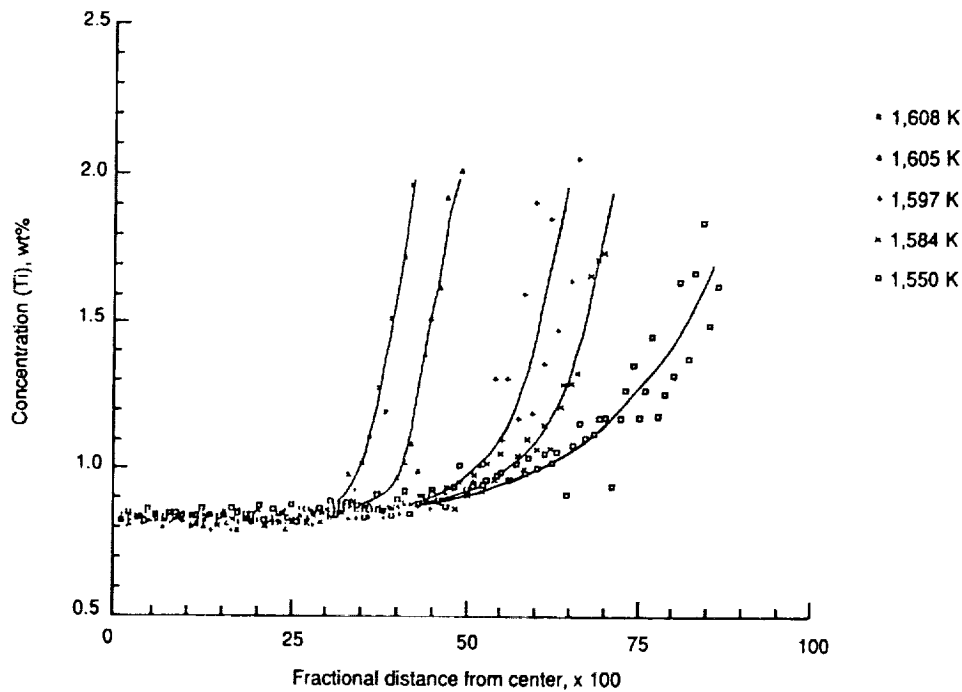


Figure 19b. Superposition of Ti solutal profiles for the transverse microstructures shown in Figure 15.

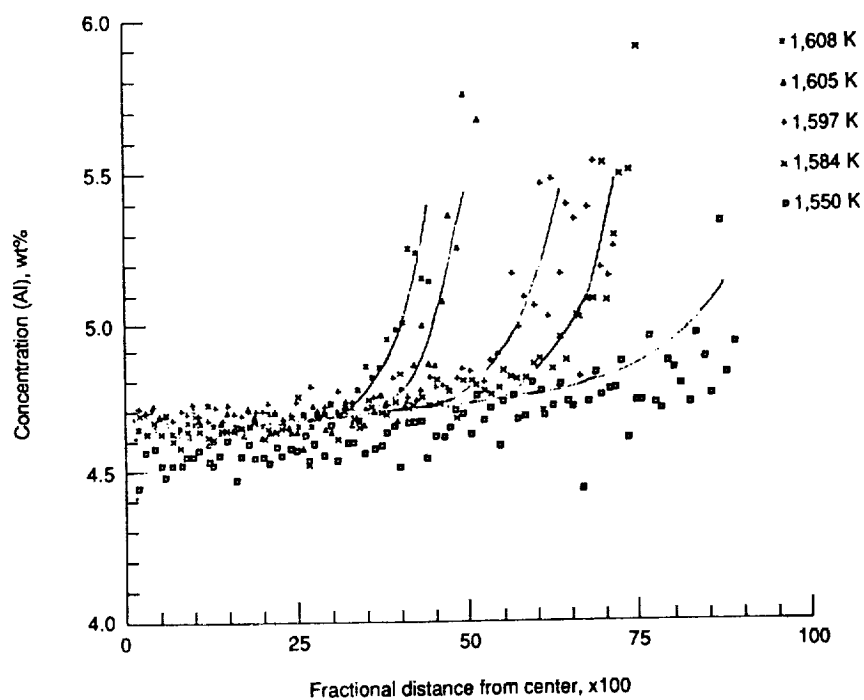


Figure 19c. Superposition of Al solutal profiles for the transverse microstructures shown in Figure 15.

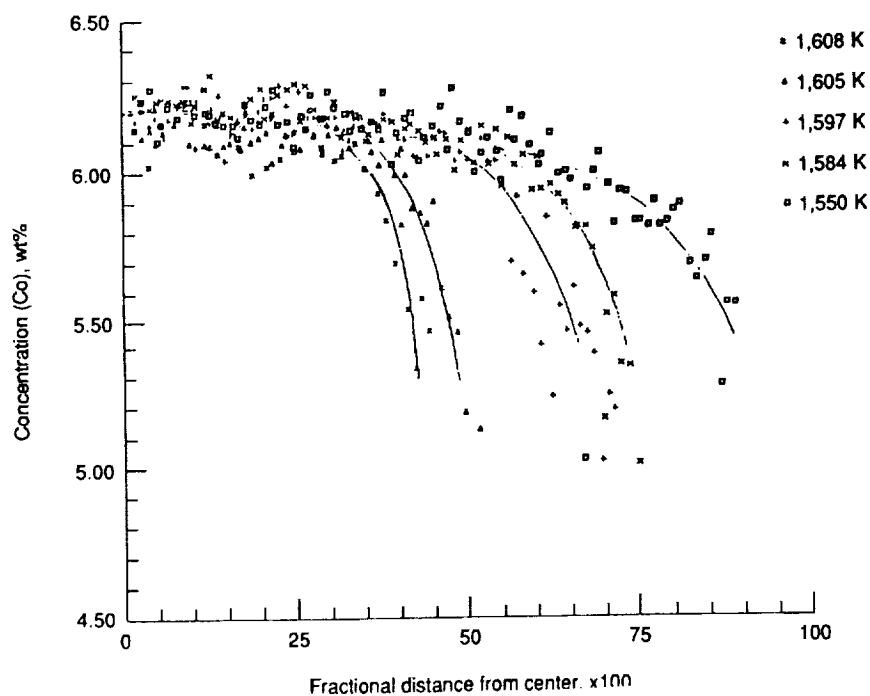


Figure 19d. Superposition of Co solutal profiles for the transverse microstructures shown in Figure 15.

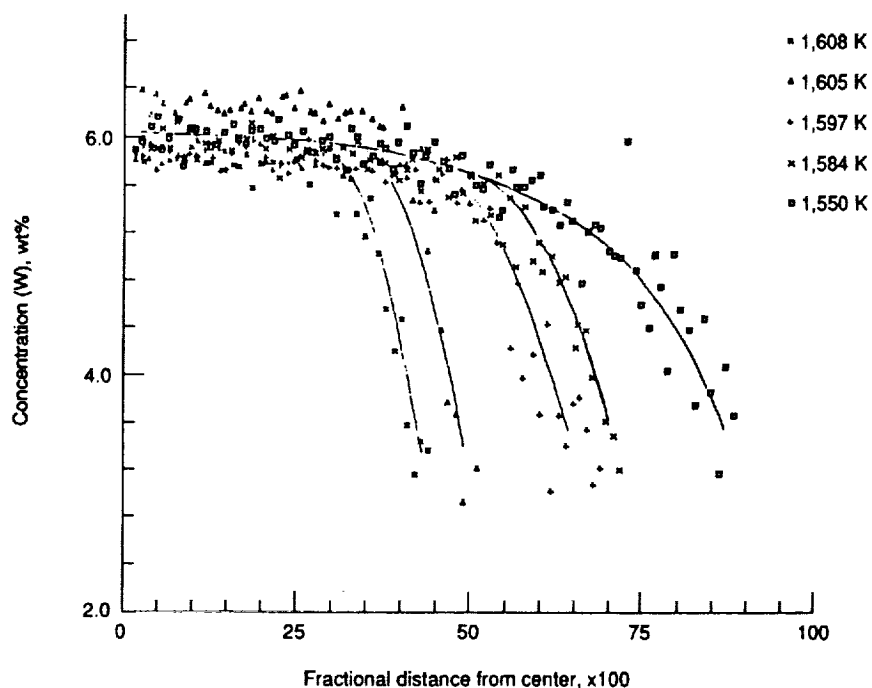


Figure 19e. Superposition of W solutal profiles for the transverse microstructures shown in Figure 15.

sections of the partially directionally solidified and quenched metallic alloy specimens cannot be used for microsegregation studies. The exception may be those growth conditions (and alloy compositions) which result in large spacing between adjacent primary dendrites (large volume fraction of the two phase eutectic-like region) at their base.

It is clear from Figures 19a to 19e that the solute contents in the dendrite core (near zero fraction solid) are nearly the same for all of the transverse sections examined in the mushy zone for all the elements studied. This indicates that the solid-state diffusion effects are negligible. In the presence of significant diffusion in the solid, the solute content at zero fraction solid would be expected to be higher for the transverse section at the base of the primary dendrite, as compared to that near the tip, for solutes having less than unity partition coefficients (Ta, Ti, and Al). The opposite would be the case for W and Co. The solid-state diffusion effects, if present, cannot be resolved with the present amount of scatter in the microsegregation data (discussed in more detail later).

### Solute Partition Coefficients

Solutal profiles obtained at several temperatures (several transverse cross sections along the length of the primary dendrites) can be used to obtain the solute partition coefficients corresponding to these temperatures, if we assume that there is no transverse solutal gradient in the interdendritic melt. This assumption has been made in all of the microsegregation models proposed in the literature. In order to obtain the partition coefficients, we require  $C_s^*$ , the composition in the solid at the surface of the primary dendrite, and  $C_l$ , the composition of the interdendritic liquid in equilibrium



at that temperature. As an example, let us consider Figures 19a to 19e, which show the superposition of the solutal profiles obtained at 1,608, 1,605, 1,597, 1,584, and 1,550 K. The solutal profile at all the temperatures in the mushy zone follow the one at the base of the dendrite until their corresponding beginning of the steep rise. This observation indicates that  $C_s^*$  at any temperature is that composition just before its solutal profile takes off for the steep rise. The corresponding composition of the interdendritic liquid ( $C_l$ ) can be obtained by integrating the remainder of the solutal profile at that temperature for compositions beyond  $C_s^*$  (including the region corresponding to the quenched interdendritic melt shown in Fig. 18) and obtaining the average value. This is schematically shown as the hatched area in the inset of Figure 18a. The  $C_l$  and  $C_s^*$  values thus obtained at several temperatures are compiled in Table 3. The partition coefficients ( $C_s^*/C_l$ ) for tantalum, titanium, aluminum, cobalt, and tungsten are also given in this table.

TABLE 3. SOLUTAL PARTITION COEFFICIENTS OF PWA-1480

T (K)	Ta			Ti			Al			Co			W		
	Cs	C <sub>l</sub>	k	Cs	C <sub>l</sub>	k	Cs	C <sub>l</sub>	k	Cs	C <sub>l</sub>	k	Cs	C <sub>l</sub>	k
1,608	8.02	12.66	0.63	0.83	1.85	0.45	4.49	4.98	0.90	6.13	5.48	1.12	5.80	3.59	1.61
1,605	8.32	14.68	0.57	0.85	2.19	0.39	4.68	5.41	0.87	6.11	5.29	1.16	6.26	3.53	1.78
1,597	8.48	13.69	0.62	0.90	2.024	0.44	4.81	5.41	0.89	6.08	5.35	1.14	5.54	3.35	1.65
1,584	8.99	14.54	0.62	1.05	2.37	0.44	4.85	5.40	0.90	6.03	5.40	1.12	5.21	3.20	1.63
	0.61±0.12			0.43±0.10			0.89±0.10			1.13±0.07			1.67±0.3		
Binary	0.44 (26)						0.54 (26)								
Superalloy				0.60 (28) mm-200 0.80 waspalloy			0.80 (27) waspalloy			1.10 (27) waspalloy			1.2 (28)		

The above technique could not be used to obtain the partition coefficients below approximately 1,584 K. The scatter in the solute composition versus fraction distance plots (such as shown in Fig. 19) becomes too large to reliably locate  $C_s^*$ , the compositions at which the steep rise in the solute contents begin. Therefore, the solute partition coefficients could not be obtained for the temperatures corresponding to the interdendritic regions closer to the base of the primary dendrites, i.e., between 1,584 and 1,550 K. An examination of Table 3 shows that the solute coefficients of all these elements are reasonably constant in the temperature range investigated here. The average partition coefficients for Ta, Al, Ti, Co, and W, are listed in Table 3. Their variations are computed on the basis of the standard variations for the  $C_s^*$  and  $C_l$  values. These partition coefficients can be compared (Table 3) with those reported in the literature for corresponding nickel-based binaries [48] and some commercial superalloys [49,50]. The average partition coefficients listed in this table will later be used to compare the experimentally observed microsegregation in directionally solidified single crystal PWA-1480 sample with predictions from simple models developed for binary alloys.

## DISCUSSION

### Growth Rate and Thermal Gradient Dependence: Comparison with Dendritic Growth Models

At high gradient of constitutional supercooling, i.e., for growth conditions where  $G_c^l$  is much larger than  $G_c$  for  $G_l/m_1$ , the dendrite tip radius predictions from dendrite growth models for binary alloys are nearly the same [6,51]. Incorporation of growth rate and thermal gradient dependence of the tip radii, as predicted from these models, in equation (1) yields the following relationship for the primary dendrite spacings.

$$\lambda_1^2 = (64 B \sigma D_l \Delta T_o / k \Delta S)^{0.25} G_l^{-0.50} R^{-0.25} \quad , \quad (3)$$

where,  $\sigma$  is the solid-liquid surface energy,  $\Delta T_o = m_1 C_o (k-1)/k$  is the alloy freezing range,  $\Delta S$  is the entropy of fusion per unit volume and  $B$  is approximately a constant. The value of  $B$  is respectively 1, 1/16 or 1/28 for the dendrite growth models of Burden and Hunt [5], Laxmanan [51], and Trivedi [3]. In the following section we will examine the growth rate and thermal gradient dependence of primary dendrite spacings data for PWA-1480, and compare them quantitatively with those expected from the above described models. Despite its multicomponent nature, PWA-1480 shows a solidification behavior which is similar to a binary alloy. Solidification of the last interdendritic eutectic liquid occurs in a very narrow temperature range (1,548 to 1,553 K); it can be considered nearly isothermal (liquidus temperature of PWA-1480 is 1,610K). The solute partition coefficients, obtained from examining their microsegregation behavior in PWA-1480, appear to be temperature independent. We will, therefore, use these models to examine their primary dendrite spacing predictions, although the models are valid only for simple binary alloys directionally solidified in a positive thermal gradient.

Figure 20 shows the thermal gradient ( $G_l$ ) and growth rate ( $R$ ) dependence of the primary dendrite spacings ( $\lambda_1$ ) in directionally solidified single crystal specimens of PWA-1480. The primary dendrite spacings shown in this figure are the values measured near the quenched end of the specimen. As mentioned earlier (Fig. 6), this was the region where steady-state growth can be assumed to have occurred. Growth speed  $R$  is assumed to be identical to the furnace withdrawal speed. The thermal gradients for each specimen are the values measured at the liquidus temperature (1,610 K) from their corresponding thermal profiles (typically shown in Fig. 3). The abscissa in this figure was selected to be  $(R, \text{cm s}^{-1})^{-0.25} (G_l, \text{K cm}^{-1})^{-0.5}$  as suggested by equation (3). The solid line in this figure, described by the following relationship, is the linear least squared fit to the data.

$$\lambda_1, \text{ m} = (-12.1 \pm 12.4) + (2,298 \pm 120) (R, \text{cm s}^{-1})^{-0.25} (G_l, \text{K cm}^{-1})^{-0.5} \quad . \quad (4)$$

A high correlation coefficient value, 0.973, with a low relative standard deviation of only 6.3 percent for the fit shows an excellent linear relationship. Thus the linear dependence of primary

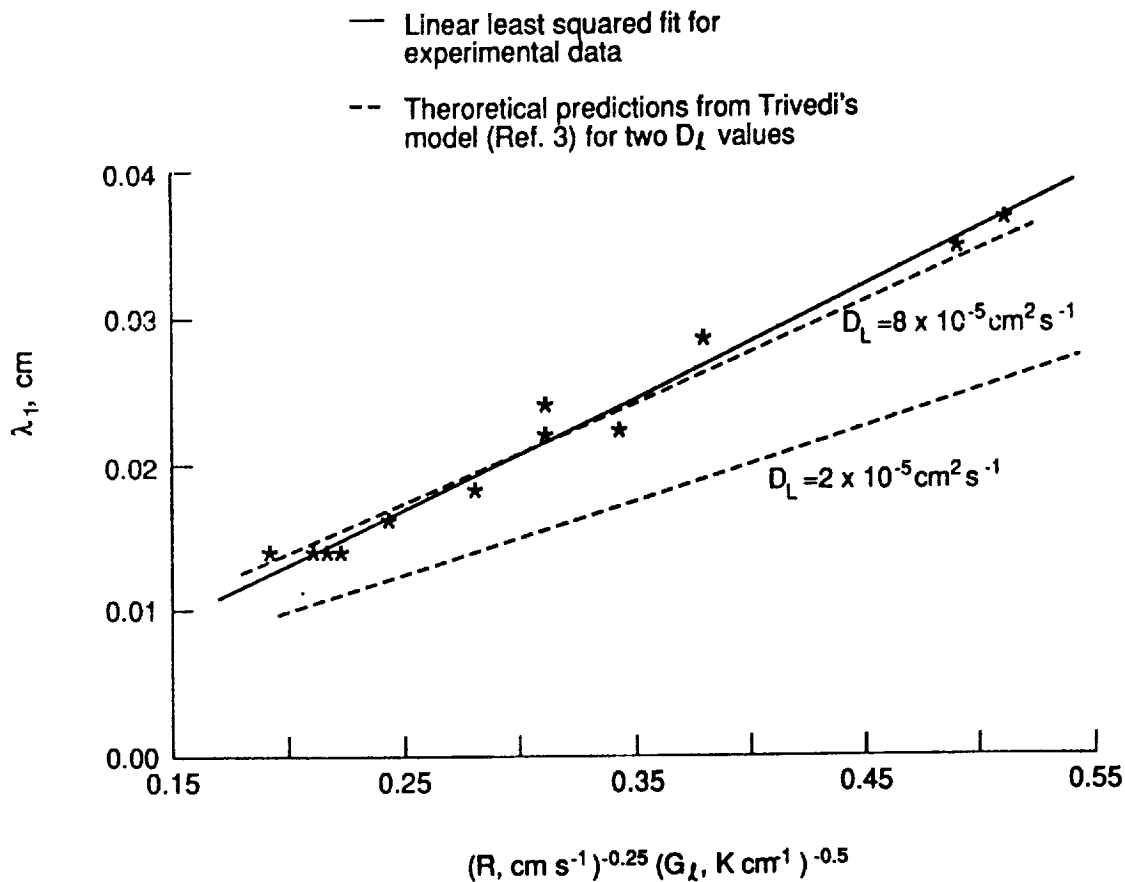


Figure 20. Thermal gradient ( $G_L$ ) and growth rate dependence of primary dendrite spacings ( $\lambda_1$ ) in directionally solidified single crystal PWA-1480.

dendrite spacings on  $G_L^{-0.5} R^{-0.25}$  predicted by the model for binary alloys due to Hunt is also valid for our complex multicomponent superalloy, PWA-1480.

We will now examine the predictions quantitatively by assuming that the dendrite spacings in PWA-1480 can be predicted by examining only one solute, for example, tantalum, i.e., by treating the alloy as if it were a binary with tantalum as solute. We will use the alloy freezing range,  $\Delta T_0 = 35 \text{ K}$  (for PWA-1480 liquidus 1,610 K, and solidus 1,575 K). The values of  $\sigma$  and the heat of fusion per unit volume for PWA-1480 will be assumed to be the same as for nickel, 255 erg/cm<sup>2</sup> [52] and  $2.77 \times 10^{10} \text{ erg/cm}^3$  [53] respectively. As mentioned earlier, the partition coefficient for tantalum in PWA-1480 is 0.6. By observing the growth conditions required for a planar solid-liquid interface during directional solidification of several superalloys, the solute diffusivities in the liquid melt were estimated to be in the range, 2 to  $8 \times 10^{-5} \text{ cm}^2 \text{ s}^{-1}$  [9]. Based on these physical parameters, the primary dendrite spacings predicted from equation 1 (or equation (3)) are plotted in Figure 20. The two broken lines in Figure 20 represent the values predicted from the approach used by Trivedi [3] for  $D_L$  values of  $2 \times 10^{-5}$  and  $8 \times 10^{-5} \text{ cm}^2 \text{ s}^{-1}$ . It should also be mentioned that the predictions obtained by combining the models due to Laxmanan [51] and Hunt [1] yield similar results (within 15 percent of the values indicated by the broken lines in Fig. 20). Considering the uncertainties in the various physical properties and the assumption of treating PWA-1480 as a binary alloy, predictions from these models are in a very good quantitative agreement with the experimental data.

A comparison of the experimentally observed tip radius of 12  $\mu\text{m}$  for one specimen,  $G_1 = 120 \text{ K cm}^{-1}$ ,  $R = 0.001 \text{ cm s}^{-1}$ , with predictions from dendrite growth models also shows a good agreement. The tip radius value predicted from the model due to Trivedi [3] is 7.2  $\mu\text{m}$  for  $D_1 = 2 \times 10^{-5} \text{ cm}^2 \text{ s}^{-1}$  and 14.4  $\mu\text{m}$  for  $D_1 = 8 \times 10^{-5} \text{ cm}^2 \text{ s}^{-1}$ .

### Side-Branch Coarsening Kinetics

Kirkwood [18] has recently proposed a simple analytical model to predict the side-branch coarsening kinetics in binary alloys. This model is well suited to partial directional solidification and quenching experiments. The analytical model assumes a constant temperature and composition for the interdendritic melt. It treats the coarsening process as a simultaneous dissolution of smaller arms (spheres) with sharper tip radii and the growth of larger arms with less curvature. The model predicts the following behavior,

$$d^3 = - [128 \sigma D_1 T/m_1 C_o (k-1) \Delta H] t \quad , \quad (5)$$

where,  $d$  is the side-branch spacing corresponding to the coarsening time  $t$  and  $\Delta H/T$  is the entropy of fusion per unit volume. The experimentally observed coarsening behavior for superalloy PWA-1480 is compared with prediction from the above relationship, considering the multicomponent superalloy to behave like a binary.

Figure 21 plots  $\log_{10}(d)$  versus  $\log_{10}(t)$  data obtained from several experiments. It contains the data from Figures 9 and 10 for the KC-135 specimens grown at 0.013 and 0.023  $\text{cm s}^{-1}$ , and also includes the data from two ground based specimens grown at 0.001 and 0.007  $\text{cm s}^{-1}$ . The straight line drawn through the data is the linear least squared fit given as,

$$\log_{10}(d, \mu\text{m}) = (1.021 \pm 0.014) + (0.325 \pm 0.010) \log_{10} (t, \text{s}) \quad .$$

For this fit, the correlation coefficient is 0.825 and the relative standard deviation is 5.2 percent. The slope of this line, 0.325, is identical to that expected from the above coarsening relationship, equation (5). The experimentally obtained value  $1.2 \times 10^{-9} \text{ cm}^3/\text{s}$ , derived from the terms in the bracket in equation (5) (obtained from the intercept on the Y-axis in Fig. 21), was used to obtain the expected  $D_1/k$  value for PWA-1480 in the following manner. The terms within the bracket can also be expressed as  $[128 (\sigma/\Delta H) (T/\Delta T_o) (D_1/k)]$ . We assumed the coarsening temperature,  $T$ , to be the liquidus temperature, 1,610 K. The  $(D_1/k)$  value obtained by fitting the above mentioned coarsening relationship to the experimental data is about  $2 \times 10^{-5} \text{ cm}^2/\text{s}$ . Experimentally observed partition coefficients for the various solutes in superalloy PWA-1480 are in the range from 0.4 to 1.7. Thus, the solute diffusivity in the PWA-1480 melt ( $D_1$ ) would be predicted to be in the range from 0.8 to  $3.4 \times 10^{-5} \text{ cm}^2/\text{s}$ . This shows a reasonable agreement with reported solutal diffusivity approximately 2 to  $8 \times 10^{-5} \text{ cm}^2/\text{s}$  [9], obtained from estimates based on the use of constitutional supercooling criteria for plain front solidification of superalloys.

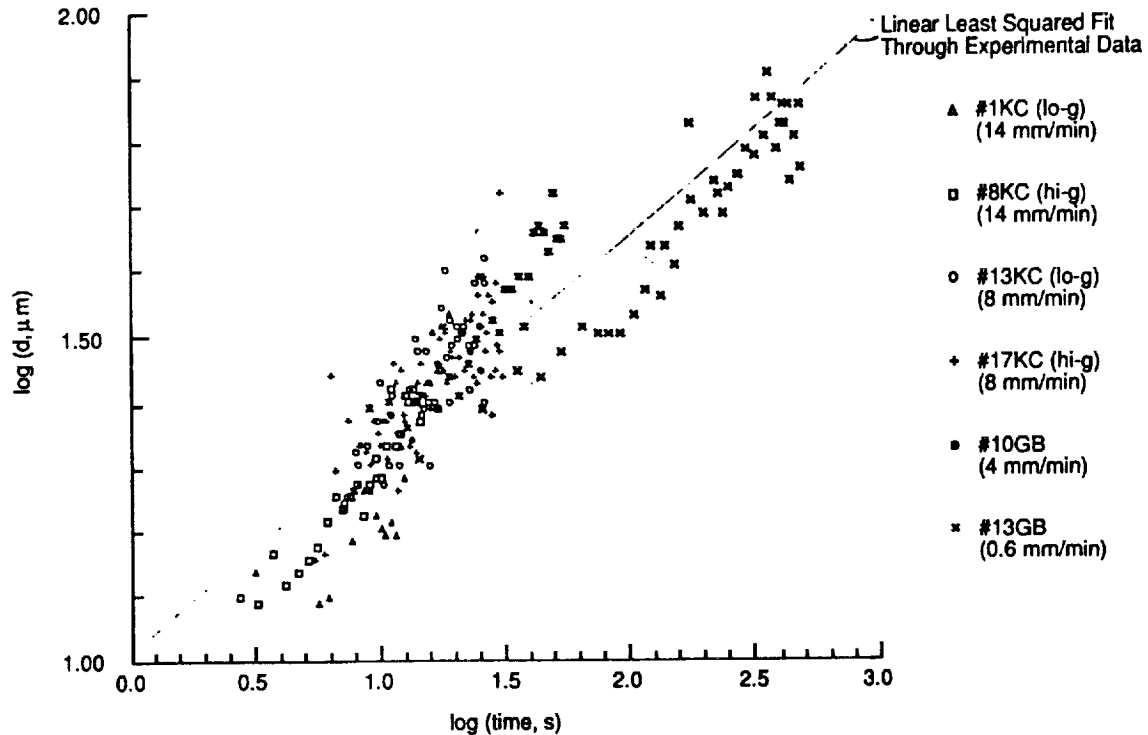


Figure 21. Side-branch coarsening kinetics in PWA-1480. The solutal diffusivity values extracted from this plot, which assumes the side-branch coarsening to obey the simple analytical model by Kirkwood [18] for a binary alloy, are in reasonable agreement with the literature reported values.

## Microsegregation

A microsegregation analysis for alloys directionally solidified with a positive thermal gradient in the melt is expected to include the following factors: the solute buildup at the dendrite tips, the solid-state diffusion, the temperature dependence of the solute partition coefficient, and the convection in the interdendritic melt due to the density difference between the solid and the liquid phases. Unfortunately, there is no theoretical (analytical or numerical) model available in the literature where all these effects have been combined in the analysis, even for a simple binary alloy. For a complex, multicomponent alloy, it is virtually impossible to consider all these effects in the analysis. Therefore, we will make several simplifying assumptions. We ignore the convection effects. Also, we will assume that there is no interaction among the various solutes, so the liquidus and the solidus profiles of the alloy can be treated for each element separately. This assumption is reasonable because the partition coefficient for each of the solutes appears to be constant, in the temperature range from 1,584 to 1,610 K. However, such a behavior is unusual and is generally not to be expected for a complex multicomponent alloy. Independent experimental study of the temperature dependence of the solute partition coefficients in PWA-1480 will, therefore, be of considerable interest.

As shown earlier, the superposition of the microsegregation profiles across several transverse sections in the interdendritic region suggests that the solid-state diffusion can be ignored for all solute elements. The literature reported temperature dependence of the elemental diffusivities in solid nickel [54] can be used to obtain an estimate of the contribution of solid-state diffusion to the microsegregation. For example, at 1,600 K the diffusivity of titanium, aluminum, and tungsten are 3.5, 1.3, and  $0.36 \times 10^{-9} \text{ cm}^2/\text{s}$ , respectively. We will utilize the numerical analysis recently developed by Yeum, Laxmanan, and Poirier [22] to estimate the contribution to the microsegregation due to the solid-state diffusion (Scheil distribution + solid-state diffusion) for titanium, which has the high diffusivity. The pre-exponential factor and the activation energy values for the diffusion of titanium in nickel [57] will be used in the numerical analysis, assuming that during solidification the temperature varies from the liquidus (1,610 K) to the eutectic temperature (1,550 K) of PWA-1480. The parameters  $C_0 = 1.35$  and  $k = 0.43$ , and the maximum dimension along "A" type path at the base of primary dendrites = 176  $\mu\text{m}$ , applicable for our single crystal PWA-1480 sample will be used. The results of this analysis are presented in Figure 22. The solid line indicates the Scheil distribution of solute. The broken line shows the microsegregation profile modified by diffusion in solid. The two microsegregation profiles are virtually indistinguishable, considering the 3 percent experimental scatters in generating the composition data described earlier. The diffusion contribution for other elements would be even less due to their much smaller diffusivities. Therefore, the solid-state diffusion contribution will not be considered in further analysis.

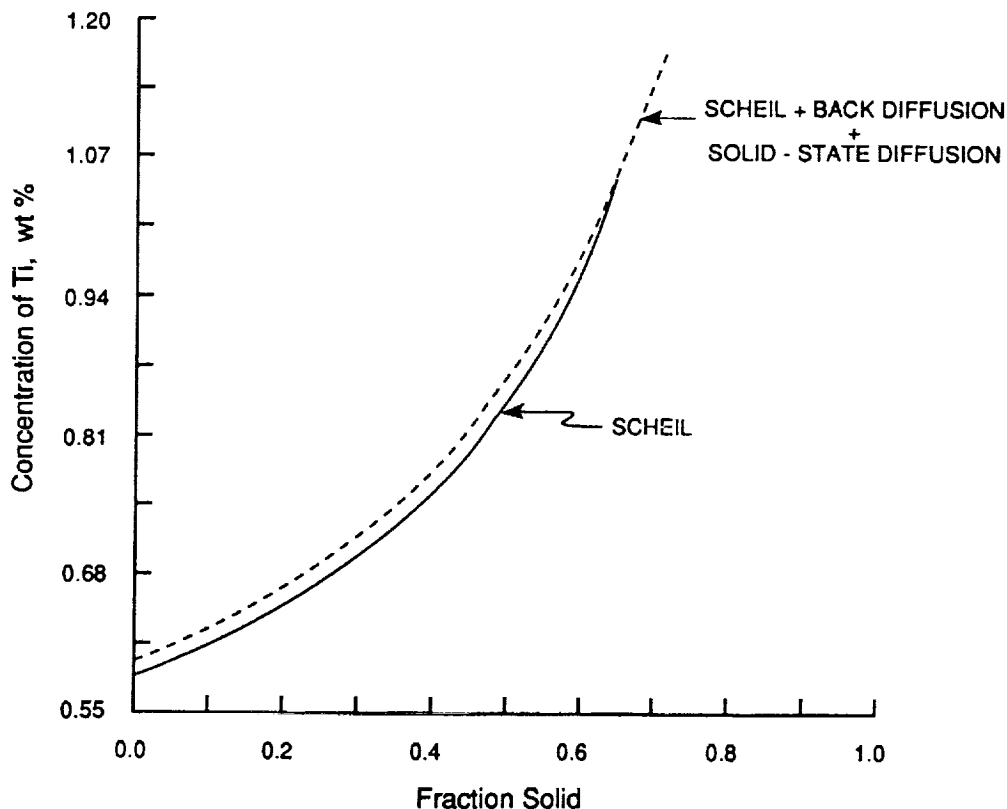


Figure 22. Estimate of the contribution of solid-state diffusion to the microsegregation of titanium in PWA-1480.

## Dendrite Tip Composition

A dimensionless parameter,  $q = [(C_t) - C_o]/[(C_o/k) - C_o]$  [55] has been used in the literature to describe the solute buildup at the dendrite tip. The solute content in the primary dendrite solid ( $C_s^*$ ) at a fraction distance from the center equal to zero ( $f_s = 0$ ) (Fig. 19) has been used to obtain  $C_t = C_s^*/k$ . An examination of  $C_t$  and  $C_o$  values (Table 4) shows that for tantalum, titanium, and aluminum, with their partition coefficients less than one, there appears to be a slight solute buildup at the tip,  $C_t > C_o$ . For tungsten there is a solute depletion,  $C_t < C_o$ , as expected due to its  $k > 1$ . For cobalt the  $C_t$  value should be less than  $C_o$  because  $k = 1.13$  is greater than unity. However, its  $C_t$  of 5.49 is more than  $C_o = 5.36$ . Any measurement inaccuracy in obtaining  $C_o$  and  $C_t$ , especially for elements whose partition coefficient is very close to one (for example, aluminum and cobalt, Table 3) will result in such an apparent anomaly. The solutal buildup ( $k < 1$ ) and depletion ( $k > 1$ ) are, however, very small (Table 3). For this growth condition, the composition of the melt at the dendrite tip is very close to the original alloy composition. There appears to be a tendency for solutal buildup for elements with  $k < 1$  or solutal depletion for  $k > 1$ . Table 4 also lists the experimentally observed values of the dimensionless parameter,  $q$ . The parameter,  $q$ , denoting the solute buildup at the tip for elements with  $k < 1$  or depletion for  $k > 1$ , as compared to the original melt composition,  $C_o$ , is a positive number, and can never be negative. The negative  $q$  value obtained for cobalt in Table 4 must be due to the measurement uncertainties in  $C_s^*$  at the tip and  $C_o$ , previously described.

TABLE 4. SOLUTAL BUILDUP AT THE DENDRITE TIP

	<b>k</b>	<b>C<sub>o</sub></b> <b>(wt%)</b>	<b>C<sub>t</sub></b> <b>(wt%)</b>	<b>q</b>	<b>s</b>	<b>a</b>
<b>Al</b>	0.89	4.91	5.11	0.33	0.33	-0.04
<b>Ti</b>	0.43	1.36	1.98	0.34	0.34	-0.45
<b>Co</b>	1.13	5.36	5.49	-0.21	-0.22	-0.02
<b>W</b>	1.67	4.08	3.62	0.28	0.27	0.11
<b>Ta</b>	0.61	11.81	13.30	0.20	0.19	-0.12

**C.V.:** Coefficient of variation; **R<sup>2</sup>:** Correlation Coefficient

An examination of the average composition ( $\bar{C}_s$ ), average of the interdendritic liquid and solid phases in the mushy zone also shows the previously described tendency for solutal buildup at the dendrite tips for Ta, Ti, and Al; and for solutal depletion for Co and W (Fig. 23). We will consider the steady-state directional solidification of a binary alloy melt in a positive thermal gradient in the absence of any macrosegregation due to the convection and assume a cellular/dendritic solid-liquid interface. The average composition of the directionally solidified solid (primary dendrite and the interdendritic two phase region) will be equal to the original alloy melt composition,  $C_o$ . Composition of the interdendritic melt will vary from the eutectic at the base of the primary dendrites to  $C_t$  at the dendrite tip. The composition of the liquid at the dendrite tip,  $C_t$ , will be higher than  $C_o$  ( $k < 1$ ) due to the solutal buildup. Solute content of the melt will decay to the original melt composition,  $C_o$ , at some distance ahead of the tip. The average composition of the solid and the interdendritic liquid,  $\bar{C}_s$ , corresponding to any given temperature in the mushy

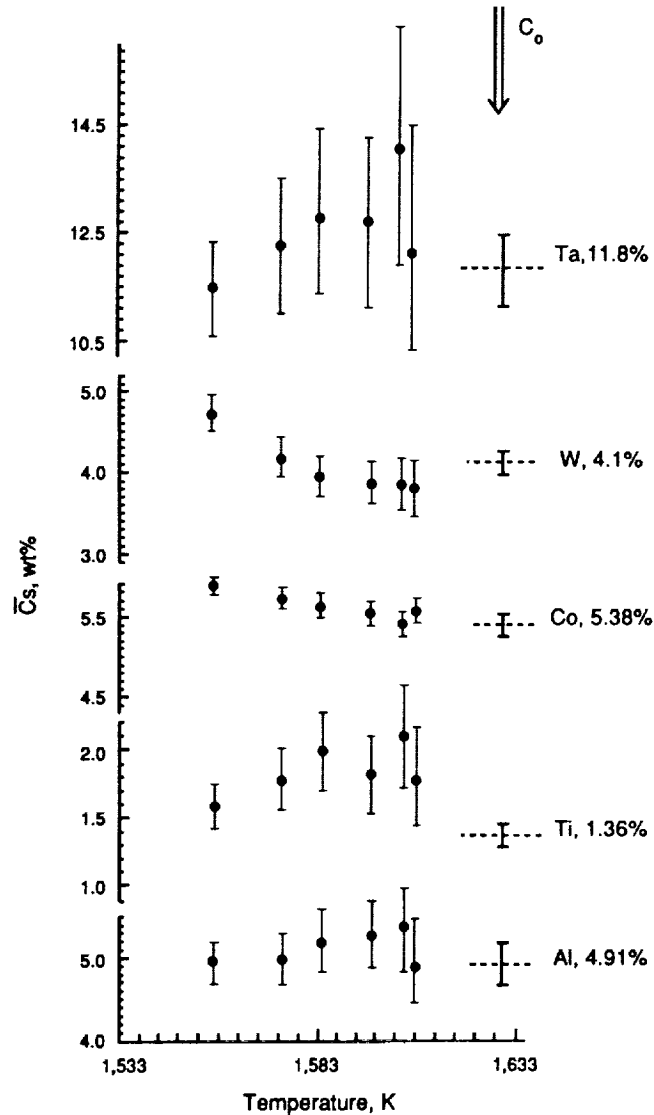


Figure 23. Variation of the  $\bar{C}_s$  (average composition of the solid and interdendritic liquid) along the length of the primary dendrite protruding above the “eutectic” temperature.

zone will be equal to  $C_0$ , only if the microsegregation can be described by the Scheil behavior [55], i.e., no diffusion of solute in the interdendritic melt and no diffusion in the solid. In the presence of solutal buildup at the dendrite tip, i.e., solutal diffusion in the interdendritic melt from the base to the tip, the  $\bar{C}_s$  value will be higher than  $C_0$ . For an alloy with a very small volume fraction eutectic at the base of the primary dendrites (directionally solidified PWA-1480 has about 5 to 8 percent volume fraction gamma-gamma prime eutectic),  $\bar{C}_s$  will be close to  $C_0$  near the eutectic isotherm at the base of the dendrite. It will increase to  $C_t$  near the dendrite tip. The experimentally observed  $\bar{C}_s$  values in the mushy zone of directionally solidified PWA-1480 are plotted in Figure 23. These  $\bar{C}_s$  values have been obtained by integrating the total area under the solute composition versus fraction distance plots obtained on the dendritic cross sections in the



mushy zone in a manner shown schematically in the inset of Figure 18. Considering the scatter and the uncertainty in the data in Figure 23, it may be argued that the  $\bar{C}_s$  values are nearly constant in the interdendritic region. However, there appears to be a trend of  $\bar{C}_s$  increasing from the eutectic temperature towards the tip for tantalum, titanium, and aluminum ( $k < 1$ ); and of  $\bar{C}_s$  decreasing for tungsten and cobalt ( $k > 1$ ). The  $C_o$  values are also shown as dotted lines in Figure 23. The relative appearance of  $\bar{C}_s$  data with respect to the  $C_o$  values in Figure 23 ( $\bar{C}_s$  values near the base of the dendrites are different from  $C_o$ ), especially for tungsten and cobalt, may appear inconsistent. However, it may be due to the uncertainty in the reported chemical analysis values for the original alloy bar stock, shown as error bars on the dotted lines corresponding to  $C_o$ . These analyses were obtained by inductively coupled plasma atomic emission spectrophotometry.

The solute buildup in the melt at the dendrite tips may be due to diffusion in the interdendritic melt from the base to the tip of the dendrite ( $k < 1$ ) and the divergent solutal field because of the tip curvature [5,51]. An examination of the following relationship proposed by Laxmanan for a "minimum undercooled dendrite" shows that for the growth conditions examined in this study, the curvature effects are negligible [51].

$$q = s + \frac{2 p k \lambda (1-s)}{1-2 p \lambda (1-k)} \quad (6)$$

In the above relationship, the Chalmers number,  $s$ , is equal to  $(D_1 G_1 / R \Delta T_o)$ ,  $G_1$  is the thermal gradient in the melt at the dendrite tip ( $120 \text{ K cm}^{-1}$ ) and  $R$  is the alloy growth speed ( $0.001 \text{ cm s}^{-1}$ ). The solutal Peclet number,  $p$ , is given by  $R r_t / 2 D_1$  and  $\lambda$  is a proportionality constant, approximately equal to  $1/16$ . The first term,  $s$ , in the above relationship is the contribution due to the diffusion in the interdendritic liquid from behind the tip, originally considered by Bower, Brody, and Flemings [4]. The second term is the contribution due to the curvature at the tip. The dendrite tip radius was approximately  $12 \text{ }\mu\text{m}$  for the PWA-1480 specimen examined in this study. Assuming a typical  $D_1$  value of about  $2 \times 10^{-5} \text{ cm}^2/\text{s}$ , the solutal Peclet number is approximately 0.03. The  $s$  values calculated from equation (6) (using the experimentally observed  $q$  values) are listed in Table 4. A comparison of the  $s$  and  $q$  values in Table 4 shows similar results, i.e., the contribution to the solutal buildup at the dendrite tip due to the tip curvature is negligible. The only significant contribution to the solute buildup at the dendrite tip is the solute diffusing from the eutectic region at the base to the tips of the primary dendrites.

The " $s$ " values listed for tantalum, titanium, aluminum, tungsten, and cobalt in Table 4 have been obtained from their experimentally observed  $C_t$  and  $C_o$  values. Disregarding the data for cobalt, because of its experimentally observed negative " $q$ " (discussed earlier), the " $s$ " values vary from 0.19 to 0.34. The average " $s$ " value is about 0.24. As previously described, the Chalmers number ( $s$ ) is defined as,  $D_1 G_1 / R \Delta T_o$ . If we assume that all the solute elements have the same diffusivity in the melt,  $D_1 = 2 \times 10^{-5} \text{ cm}^2/\text{s}$ ; the " $s$ " value will depend only upon the alloy growth parameters. For the current specimen ( $G_1 = 120 \text{ K cm}^{-1}$ ,  $R = 0.001 \text{ cm s}^{-1}$  and  $\Delta T_o = 35 \text{ K}$ ), the " $s$ " value should be about 0.1. Considering the uncertainty in the  $D_1$  value, the " $s$ " value of 0.1 compares favorably with the experimentally observed average of approximately 0.24. It also suggests that the only contribution to the solutal buildup at the dendrite tip is due to the diffusion in the interdendritic melt from behind the dendrite tip.

## Microsegregation Profile

Due to the negligible curvature contribution to the dendrite tip composition and the other previously described assumption, the simple microsegregation model of Bower, Brody, and Flemings [4] can be used to analyze the solutal microsegregations observed in the PWA-1480 specimen. The following relationship has been proposed by Bower, Brody, and Flemings for microsegregation in a binary alloy [1].

$$C_s^* = kC_o \{a/(k-1) + [1 - ak/(k-1)] (1-f_s)^{(k-1)}\} \quad (7)$$

where,  $C_i = C_o (1-a)$ . The parameter "a" is related to Chalmers number (s) previously described by "s" =  $ak/(k-1)$ . The values for the "a" parameters experimentally obtained from their corresponding  $C_i$  and  $C_o$  are listed in Table 4. Figure 24 shows the correlation between the experimentally observed solutal profiles across the primary dendrites at their base (1,550 K) and the theoretical predictions derived from the model of Bower, Brody, and Flemings. The data in these figures are the elemental composition,  $C_s^*$ , versus the fraction solid,  $f_s$ , obtained utilizing the previously described methodology. The solid lines are the predictions from equation (7). The theoretical predictions are in good agreement with the experimental data for tantalum, aluminum, cobalt, and tungsten. The agreement is poorer for titanium. In general, the agreement is better for fraction solid less than 50 to 60 percent (corresponding to the values of fraction distance from the center of the primary dendrite being less than 70 to 75 percent). For previously described reasons, the solute partition coefficients were not measured at temperatures below 1,584 K in this investigation. It is possible that the partition coefficients are not constant in this temperature range, which would correspond to the higher fraction solid, as is presently assumed. An independent experimental determination of the solute partition coefficients is required to investigate this possibility. For reasons previously discussed, the higher fraction solid portion is also the region of increased scatter in the data [24].

## CONCLUSIONS

The following conclusions can be drawn from this study on PWA-1480 single crystal superalloy specimens directionally solidified on the ground and during low gravity (25 s) and high gravity (60 to 90 s) periods of the KC-135 aircraft parabolic maneuvers. These specimens were rapidly quenched after partial directional solidification to retain the mushy-zone microstructure and the solutal distributions.

(1) PWA-1480, despite being a multicomponent complex superalloy, has a solidification behavior very similar to that of a binary alloy. This can be attributed to the nearly isothermal eutectic solidification (a very narrow range of about 5 K) and the absence of formation of any interdendritic phase before eutectic solidification.

(2) The specimen length used in this study, approximately 7 cm, with the melt portion varying from 2 to 5 cm, is not sufficient to achieve ideal thermal steady-state growth conditions.

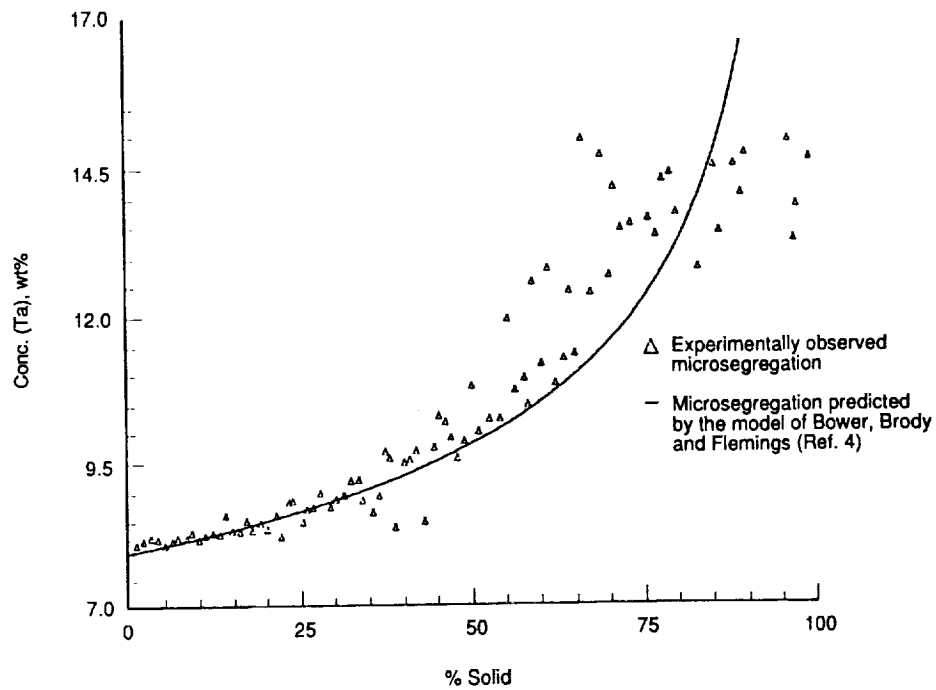


Figure 24a. Comparison of the experimentally observed Ta microsegregation with the microsegregation predicted by the model of Bower, Brody, and Flemings [4].

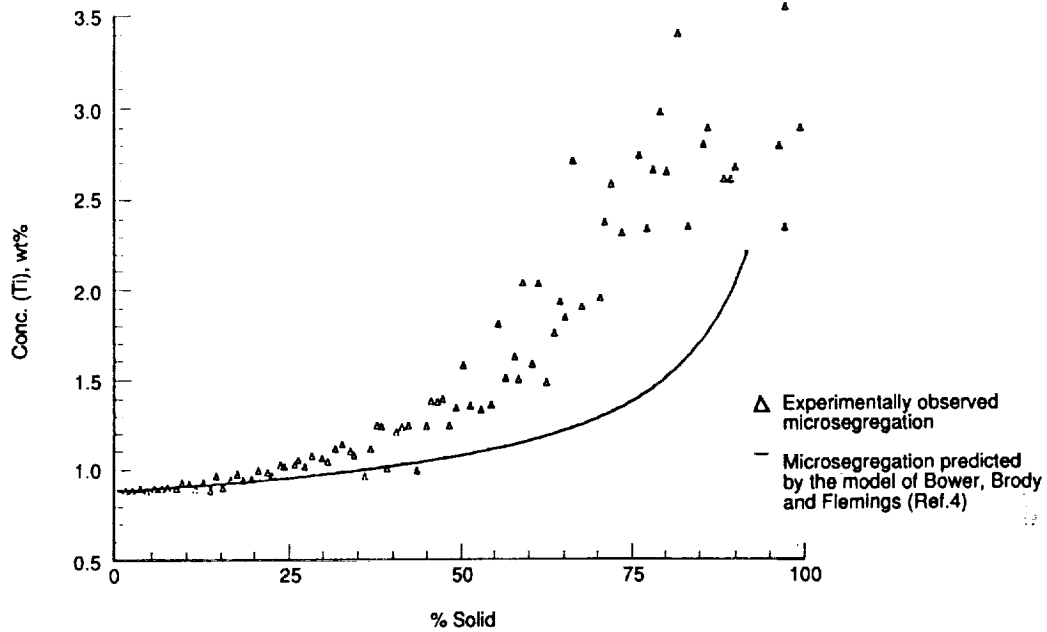


Figure 24b. Comparison of the experimentally observed Ti microsegregation with the microsegregation predicted by the model of Bower, Brody, and Flemings [4].

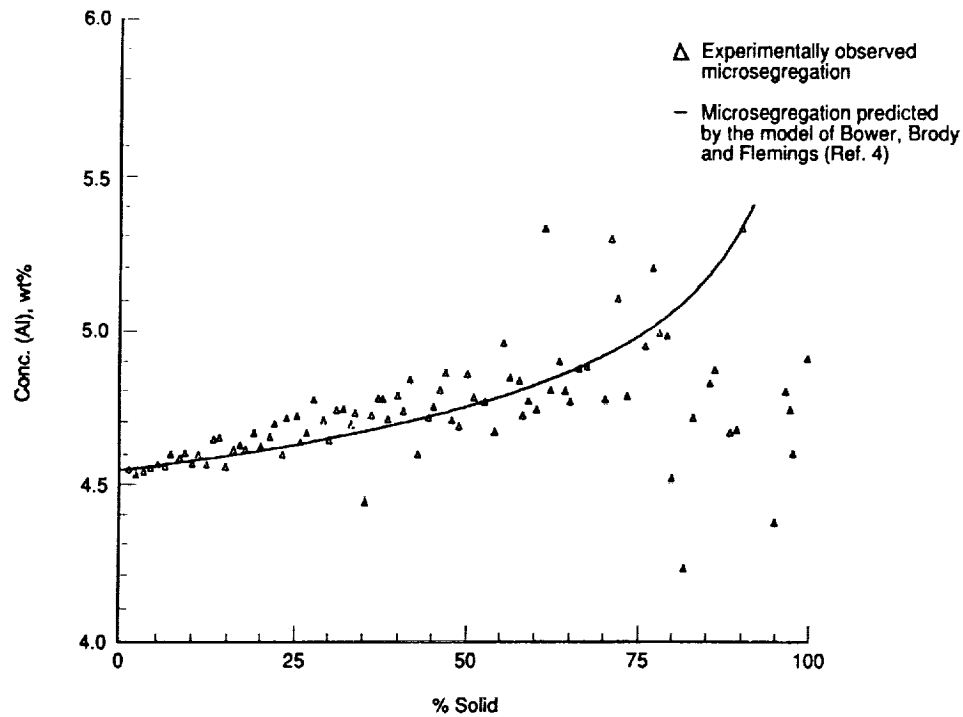


Figure 24c. Comparison of the experimentally observed Al microsegregation with the microsegregation predicted by the model of Bower, Brody, and Flemings [4].

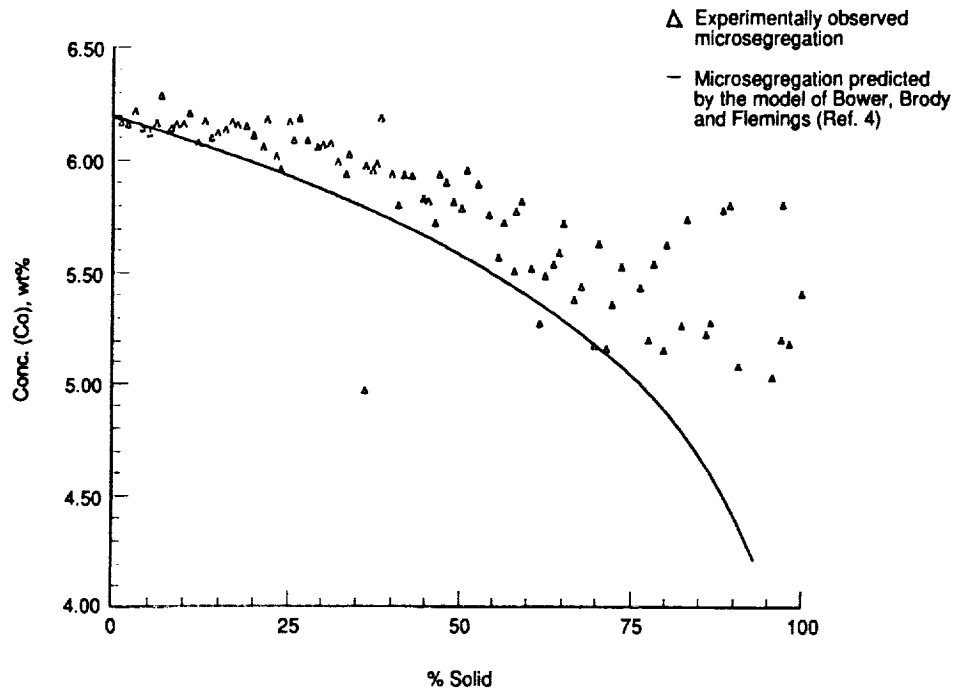


Figure 24d. Comparison of the experimentally observed Co microsegregation with the microsegregation predicted by the model of Bower, Brody, and Flemings [4].

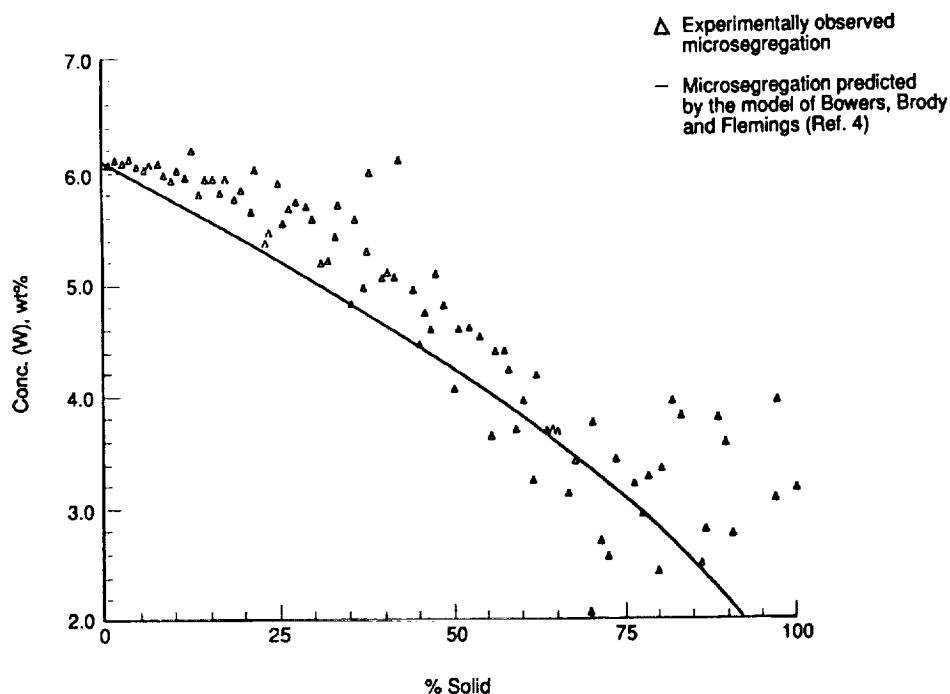


Figure 24e. Comparison of the experimentally observed W microsegregation with the microsegregation predicted by the model of Bower, Brody, and Flemings [4].

Examination of the primary dendrite arm spacing variation along the sample length suggests that an approximate steady-state growth was achieved for a length of only two to three times the cell length (length of the primary dendrite array in the mushy zone).

(3) The growth rate and thermal gradient dependence of primary dendrite spacings is quantitatively predicted by combining the dendritic growth models of Trivedi [3] or Laxmanan [51] with the arm spacing model of Hunt [1].

(4) Measurement of the side-branch spacing along the length of the primary dendrites, from their quenched tip to their base, shows that the secondary arm coarsening kinetics in PWA-1480 is in reasonable agreement with the behavior predicted from the simple analytical model of Kirkwood [18], developed for binary alloys.

(5) The quenched interdendritic liquid region in the mushy zone (from the base of the primary dendrites to their tip) for the longitudinal section of the directionally solidified sample cannot be used for the microsegregation study.

(6) Isoconcentration contours on transverse sections of the primary dendrites have shown that the relationship between fraction solid and the corresponding solute content in the primary dendrite at the solid-liquid interface can be accurately obtained. This is accomplished by passing a microprobe beam trace along a path from one end of the interdendritic eutectic to the other end, intersecting the core of the dendrite.

(7) Similar to their nickel based binaries, the partition coefficients for tantalum, titanium, and aluminum are less than unity, and for cobalt and tungsten are greater than unity. The solute partition coefficients appear to be independent of the temperature from 1,584 to 1,610 K.

(8) For the growth conditions of  $G_1 = 120 \text{ K cm}^{-1}$  and growth speed  $= 0.001 \text{ cm s}^{-1}$ , the contribution of solid-state diffusion to microsegregation is negligible. There appears to be a small contribution to the microsegregation from the solutal diffusion in the interdendritic melt from the base to the tips of the primary dendrites. This is indicated by the solute buildup for Ta, Ti, and Al, and solute depletion for Co and W at the dendrite tip as compared to the melt composition; and by the variation of  $\bar{C}_s$ , the average composition of the primary dendritic solid and the interdendritic liquid, in the mushy region.

(9) The experimentally observed microsegregation profiles generally follow the predictions from the model of Bower, Brody, and Flemings developed for binary alloys. However, an independent measurement of the temperature dependence of the solute partition coefficients will provide a closer examination of this correlation.

(10) The transitions from the high gravity to the low gravity periods do not correspond with any change in primary dendrite spacings. The specimen length which can be solidified during the low gravity period available during a KC-135 parabola is much smaller than the mushy zone length of PWA-1480. Specimen lengths which are three to four times the cell length need to be solidified in low gravity to ascertain the effect of microgravity. This requires access to space.

(11) Because of the insufficient low gravity time, no definite conclusions can be made about the effect of gravity on the secondary arm spacing. At higher growth rates,  $0.023 \text{ cm s}^{-1}$ , there appears to be a trend of decreasing secondary arm spacing with a transition from the high gravity to the low gravity periods of the flight. However, there is a large scatter in the data at higher growth speeds. Experiments at growth speeds less than  $0.001 \text{ cm s}^{-1}$  are required to draw definitive conclusions about the effect of low gravity on side-branch coarsening kinetics. These experiments are feasible only in the extended microgravity environment offered by space.

## REFERENCES

1. Hunt, J.D.: "Solidification and Casting of Metals." Book 192, The Metals Society, London, 1979, pp. 3-9.
2. Kurz, W., and Fisher, D.J.: *Acta Metall.*, Vol. 29, 1981, pp. 11-22.
3. Trivedi, R.: *Metall. Trans. A*, Vol. 15A, 1984, pp. 977-982.
4. Bower, T.F., Brody, H.D., and Flemings, M.C.: *Trans. Am. Inst. Min. Engrs.*, Vol. 236, 1966, pp. 624-634.
5. Burden, M.H., and Hunt, J.D.: *J. Cryst. Growth*, Vol. 22, 1974, pp. 99-108.
6. Tewari, S.N., and Laxmanan, V.: *Acta Metall.*, Vol. 35, 1987, pp. 175-183.
7. Miyata, Y., Suzuki, T., Uno, J.I.: *Metall. Trans. A*, Vol. 16A, 1985, pp. 1799-1805.
8. Geying, A., and Lixin, L.: *J. Cryst. Growth*, Vol. 80, 1987, pp. 383-392.
9. Quested, P.N., and McLean, M.: *Mat. Sci. Eng.*, Vol. 65, 1984, pp. 171-180.
10. Tewari, S.N., and Sriramamurthy, A.M.: *Metall. Trans. A*, Vol. 12A, 1980, pp. 137-138.
11. Somboonsuk, K., Mason, J.T., and Trivedi, R.: *Metall. Trans. A*, Vol. 15A, 1984, pp. 967-975.
12. Tewari, S.N., Nesarikar, V.V., and Lee, D.: "Side-Branch Morphology and Coarsening in Directionally Solidified Pb-8.4 at% Au." To appear in *Metall. Trans. A*.
13. Huang, S.C., and Glicksman, M.E.: *Acta Metall.*, Vol. 29, 1981, pp. 701-711.
14. Kattamis, T.Z., Coughlin, J.C., and Flemings, M.C.: *Trans. Amer. Inst. Met. Engr.*, Vol. 239, 1967, pp. 1504-1511.
15. Kahlweit, M.: *Scripta Metall.*, Vol. 2, 1968, pp. 251-254.
16. Young, K.A., and Kirkwood, D.H.: *Metall. Trans. A*, Vol. 6A, 1975, p. 197.
17. Curreri, P.A., Lee, J.E., and Stefanescu, D.M.: *Metall. Trans. A*, Vol. 19A, 1988, pp. 2671-2676.
18. Kirkwood, D.H.: *Materials Sci. Eng.*, Vol. 73, 1985, pp. L1-L4.
19. Brody, H.D., and Flemings, M.C.: *Trans. AIME*, Vol. 236, 1966, pp. 615-624.
20. Clyne, T.W., and Kurz, W.: *Metall. Trans.*, Vol. 12A, 1981, pp. 965-971.

21. Kobayashi, S.: *J. Cryst. Growth*, Vol. 88, 1988, pp. 87–96.
22. Yeum, K.S., Laxmanan, V., and Poirier, D.R.: “An Efficient Estimation of Solute Redistribution During Dendritic Solidification with Diffusion in Solid.” (Paper under preparation.)
23. Solari, M., and Biloni, H.: *J. Cryst. Growth*, Vol. 49, 1980, p. 451.
24. Katgerman, L.: *Scripta Metall.*, Vol. 17, 1983, pp. 537–540.
25. Sarreal, J.A., and Abbaschian, G.J.: *Metall. Trans. A*, Vol. 17A, 1986, pp. 2063–2073.
26. Sharp, R.M., and Flemings, M.C.: *Metall. Trans.*, Vol. 4B, 1973, pp. 997–1001.
27. Biloni, H., and Bolling, G.F.: *Trans. AIME*, Vol. 227, 1963, pp. 1351–1360.
28. Michael, A.B., and Bever, M.B.: *J. Metals*, 1954, pp. 1323–1325.
29. Weinberg, F., and Teghtsoonian, E.: *Metall. Trans. A*, Vol. 3, 1972, pp. 93–111.
30. Tewari, S.N.: *Metall. Trans. A*, Vol. 19A, 1988, pp. 1351–1363.
31. Kadalbal, R., Montoya-Cruz, J.J., and Kattamis, T.Z.: *Metall. Trans. A*, Vol. 11A, 1980, pp. 1547–1553.
32. Roosz, A., Simon, M., and Exner, H.E.: “Solidification Processing 87.” Conference at Sheffield, United Kingdom, September 21–24, 1987.
33. Oglvy, A.J.W., and Kirkwood, D.H.: *Applied Scientific Research*, Vol. 44, 1987, pp. 43–49.
34. Sellamuthu, R., and Goldstein, J.I.: *Metall. Trans. A*, Vol. 16A, 1985, pp. 1871–1878.
35. Kattamis, T.Z., and Flemings, M.C.: *Trans. AIME*, Vol. 233, 1965, pp. 992–999.
36. Howe, A.A., and Kirkwood, D.H.: *Applied Scientific Research*, Vol. 44, 1987, pp. 125.
37. Johnston, M.H., Curreri, P.A., Parr, R.A., and Alter, W.S.: *Metall. Trans. A*, Vol. 16A, 1985, pp. 1683–1687.
38. Johnston, M.H., and Griner, C.S.: *Metall. Trans. A*, Vol. 8A, 1977, pp. 77–82.
39. Johnston, M.H., and Parr, R.A.: *Metall. Trans. B*, Vol. 13B, 1982, pp. 85–90.
40. Stefanescu, D.M., Curreri, P.A., and Fiske, M.R.: *Metall. Trans. A*, Vol. 17A, 1986, pp. 1121–1130.



41. Tensi, H.M., and Schmidt, J.J.: "Scientific Results of the German Spacelab Mission D1." P.R. Sahm, R. Jensen, and M.H. Keller (editors), DFVLR, Germany, 1987, Chs. 4 and 5.
42. Favier, J.J., Berthier, J., Arragon, Ph., Malmejac, Y., Khryapov, V.T., and Barmin, I.V.: *Acta. Astronautica*, Vol. 9, 1982, pp. 255–259.
43. Camel, D., Favier, J.J., Dupouy, M.D., and Le Maguet, R.: "Scientific Results of the German Spacelab Mission D1." P.R. Sahm, R. Jansen, and M.H. Keller (editors), DFVLR, Germany, 1987, pp. 236–246.
44. McKay, M.H., Lee, J.E., and Curreri, P.: *Metall. Trans. A*, Vol. 17A, 1986, pp. 2301–2303.
45. Smith, G.A., and Workman, G.: "Operational Procedure and Specification for the KC-135 Automatic Directional Solidification Furnace Reference." NASA Contract Report NAS-8-34530, 1985.
46. Henoc, J., Heinrich, K.F.J., and Mykblebust, R.L.: NBS Technical Note 769, 1973.
47. Doherty, J.E., Kear, B.H., and Giamei, A.F.: *J. Metals*, 1971, pp. 59–62.
48. *Metals Handbook*, Vol. 8, 8th Edition, American Society for Metals, Metals Park, Ohio, 1973, pp. 258, 262, 291, 326.
49. Jeanfils, C.L., Chen, J.H., and Klein, H.J.: in "Modeling of Casting and Welding Processes." H.D. Brody and D.A. Apelian (editors), TMS-AIME, Warrendale, Pennsylvania, pp. 313–332.
50. Sellamuthu, R.: Ph.D. Thesis, University of Pittsburgh, Pittsburgh, Pennsylvania, 1979.
51. Laxmanan, V.: *J. Cryst. Growth*, Vol. 83, 1987, pp. 391–402.
52. Holloman, J.H., and Turnbull, D.: *Progr. Met. Phys.*, Vol. 4, 1953, pp. 333.
53. Geiger, G.H., and Poirier, D.R.: "Transport Phenomena in Metallurgy." Addison Wesley Publishing, 1972, p. 580.
54. Swalin, R.A., and Martin, A.: *Trans. AIME*, May 1956, pp. 567–572.
55. Laxmanan, V.: "Processing of Structural Metals by Rapid Solidification." American Society for Metals, No. 8619–006, 1987.
56. Laxmanan, V.: *Acta Metall.*, Vol. 33, 1985, pp. 1023–1037.

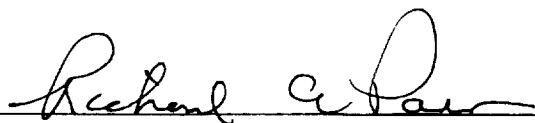


## APPROVAL

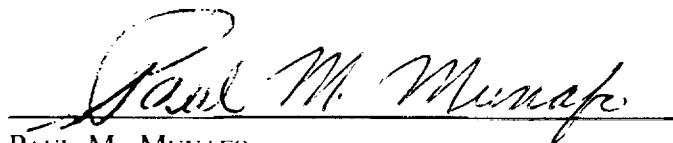
### DENDRITIC MORPHOLOGY AND MICROSEGREGATION IN DIRECTIONALLY SOLIDIFIED SUPERALLOY, PWA-1480, SINGLE CRYSTAL: EFFECT OF GRAVITY — CENTER DIRECTOR'S DISCRETIONARY FUND REPORT

By S.N. Tewari, M. Vijaya Kumar, J.E. Lee, and P.A. Curreri


The information in this report has been reviewed for technical content. Review of any information concerning Department of Defense or nuclear energy activities or programs has been made by the MSFC Security Classification Officer. This report, in its entirety, has been determined to be unclassified.



RICHARD A. PARR  
Chief, Metallurgical and Failure Analysis Branch



PAUL M. MUNAFO  
Chief, Metallic Materials Division



PAUL H. SCHUERER  
Director, Materials and Processes Laboratory

